DOKUZ EYLÜL UNIVERSITY

GRADUATE SCHOOL OF NATURAL AND APPLIED

SCIENCES

THE PRODUCTION, CHARACTERIZATION AND APPLICATION OF POLYMER BASED COMPOSITES REINFORCED BY NANOPARTICLES

by

Aylin GÜRBÜZ

June, 2009

İZMİR

THE PRODUCTION, CHARACTERIZATION AND APPLICATION OF POLYMER BASED COMPOSITES REINFORCED BY NANOPARTICLES

A Thesis Submitted to the
Graduate School of Natural and Applied Sciences of Dokuz Eylül University
In Partial Fulfillment of the Requirements for the Degree of Master of Science
in Metallurgical and Materials Engineering, Metallurgical and Materials
Program

by
Aylin GÜRBÜZ

June, 2009
İZMİR

M.Sc THESIS EXAMINATION RESULT FORM

We have read the thesis entitled **"THE PRODUCTION CHARACTERIZATION AND APPLICATION OF POLYMER BASED COMPOSITES REINFORCED BY NANOPARTICLES"** completed by **AYLİN GÜRBÜZ** under supervision of **ASSOC. PROF. DR. İSMAİL ÖZDEMİR** and we certify that in our opinion it is fully adequate, in scope and in quality, as a thesis for the degree of Master of Science.

…………………………………………

Assoc. Prof. Dr. İsmail ÖZDEMİR

―――――――――――――――

Supervisor

...………………………………… …………………………………………

Assoc. Prof. Dr. Erdal ÇELİK Assist. Prof. Dr. Aysun AKŞİT

――――――――――――――― ―――――――――――――――

(Jury Member) (Jury Member)

―――――――――――――――

Prof. Dr. Cahit HELVACI

Director

Graduate School of Natural and Applied Sciences

ACKNOWLEDGEMENTS

THE PRODUCTION, CHARACTERIZATION AND APPLICATION OF POLYMER BASED COMPOSITES REINFORCED BY NANOPARTICLES

ABSTRACT

The objective of this study is to focus on production, characterization and application areas of magnetic polymer nanocomposites. With this approach barium hexaferrite powders having nano sized particles were firstly produced by sol-gel method. Mn, Cu, Co, Sr and Ni were doped to the raw materials to investigate the effects on the magnetic, physical and chemical properties of the dopants. After preparing barium hexaferrite powders, polymer nanocomposites were prepared with the brabender machine. Then they were cured in hot pres at 160°C for 10 minutes in order to obtain highly powder dispersed nanocomposites.

Thermal behavior of barium hexaferrite powders was evaluated using Differential Thermal Analysis- Thermal Gravimetry Analysis (DTA-TGA). The surface morphology and phase identification of barium hexaferrite powders and polymer nanocomposites was performed by scanning electron microscopy (SEM) and X-Ray Diffraction (XRD), respectively. Mechanical properties such as elasticity modules and hardness of the polymer nanocomposites were also investigated through Dinamic Ultra Hardness (DUH). Hysteresis loops of barium hexaferrite powders and polymer nanocomposites, which explain magnetic properties, were obtained from Vibrating Sample Magnetometer (VSM).

As a results, it was found that hexagonal shaped powders were mostly obtained by doping Sr. In addition to improved structural morphology, it was determined that the coercivity of magnetic materials was decreased by adding doping elements. Coercivity values of undoped and doped barium hexaferrite powders were 1381.8 oersted and 500 oersted, respectively.

Keywords: Barium hexaferrite, sol-gel method, polymer nanocomposites, magnetic nanoparticles

NANO PARTİKÜL KATKILI POLİMER ESASLI NANOKOMPOZİTLERİN ÜRETİMİ, KARAKTERİZASYONU VE UYGULAMASI

ÖZ

Bu çalışmanın hedefi manyetik polimer nanokompozitlerin üretimi, karakterizasyonu ve uygulamasıdır. Bu yaklaşımla, baryum hegzaferrit tozları nanoboyutta toz elde etmek için sol-gel yöntemi ile üretilmiştir. Mn, Cu, Co, Sr ve Ni dopantlar, ham barium hegzaferrit içine fiziksel, kimyasal ve manyetik etkilerini incelemek için katılmıştır. Barium hegzaferrit tozlarını elde ettikten sonra polimer nanokompozitler brabender cihazı ile hazırlanmıştır. Yüksek sıcaklıkta tanelerin polimerin içinde homojen bir şekilde dağılması için sıcak pres işlemi 10 dk. 160 ^{o}C ve 5.5 MPa' da gerçekleştirilmiştir.

Baryum hegzaferrit tozlarının termal davranışları Diferansiyel Termal Analiz-Termal Gravimetrik Analiz (DTA-TGA) ile incelenmiştir. Baryum hegzaferrit tozlarının ve polimer nanokompozitlerin. yüzey morfolojileri ve faz tanımlaması sırasıyla Taramalı Elektron Mikroskobu (SEM) ve X-Işını Kırınımı (XRD) ile yapılmıştır. Polimer nanokompozitlerin elastisite modülü ve sertlik gibi mekanik özellikleri Dinamik Ultra Sertlik (DUH) ile araştırılmıştır. Baryum hegzaferrit tozlarının ve polimer nanokompozitlerin manyetik özelliklerini ifade eden hysteresis eğrileri VSM ile elde edilmiştir.

Sonuç olarak hegzagonal yapıdaki tozların çoğunlukla Sr katkısı ile elde edildiği bulunmuştur. Gelişmiş yapısal morfolojiye ilave olarak manyetik malzemelerin koersivite değerlerinin dopant elementleri ile düştüğü tespit edilmiştir. Ayrıca katkılı ve katkısız baryum hegzaferrit tozların sırasıyla koersivite değerleri 1381.8 oersted ve 500 oersted olduğu bulunmuştur.

Anahtar Sözcükler: baryum hegzaferrit, sol-gel metodu, polimer nanokompozitler, manyetik nanoparçacıklar

CONTENTS

CHAPTER THREE–PRODUCTION OF POLYMER NANOCOMPOSITES 30

CHAPTER ONE

INTRODUCTION

Nowadays, nanocomposites are assumed to be most charming materials due to plenty of applications such as sensors, quantum nano-electronic devices and magnetic recording materials. The nanocomposites can be formed by combining an organic polymer or inorganic such as whiskers, nanoparticles or platelets. Excellent properties given to the materials can be achieved by filling the inclusions in a host matrix. Moreover, nanocomposites materials consist of oxides conducting polymers brought out more fields of applications. In nanocomposite systems, polymers are generally used because of their molecular weight, length of chain, ease of production, ductile nature and functional groups. By considering this approach, it is probable to improve polymer properties that maintains their light weight and ductile nature. Polymer nanocomposites including spheres, rods and plates are dispersed in polymer matrix that have been increased substantial academic and industrial interest since their beginning. (Jordan, Jacob, Tannenbaum, Sharaf & Jasiuk, 2005; Gupta et al., 2008; Winey & Vaia, 2007).

Composite materials are generally independent of the size of the fillers. Yet this phenomenon is not correct for nanocomposite systems (Gacitua, Ballerini & Zhang, 2005). The smaller the reinforcing composites elements are, the larger is their international surface. In addition nanopowders have tendency to agglomerate rather than to disperse homogenously in a matrix. In most cases, the natural agglomeration tendency of the nano particles has either been difficult to overcome or led to thermodynamically instable mixtures. In such systems, three components have to be considered: interfacial component (surfactant), particle (surface), and the matrix polymer chains. It is also stated that entropy loss of the gap between particles (sheets) and the penetrated polymer coils will be approximately compensated by the entropy gain of the surfactant molecules that has an interaction with polymer chains.

One can understand from this statement that the interaction enthalpy between the surfactant molecules and the polymer chain might be decided a value for a

thermodynamically stable, homogenous incorporation (agglomeration) of nano particles into a matrix material (Fischer, 2003).

We can describe magnetic polymer nanocomposites which are composed of in organic magnetic component such as particles, fibers or lamella in the nanometer range (1-100) embedded in a organic polymer. In a composite material, the main idea is to integrate different properties in one material. To constitute synergy by assembling organic- inorganic components that cannot be obtained with neither organic nor inorganic, the structure and magnetic properties of magnetic filler reinforced polymer nanocomposites have been studied in a wide range of research areas.

Polychloroprene as a elastomeric matrix is especially used for naval applications due to the sea water resistance. Substituted barium hexaferrite powders were embedded in this matrix by compression molding with a ratio of 80:20 (barium hexaferrite: polychloprene). After that, magnetic properties of this composite were investigated. The H_c of the composites was found 800 kOe. (Pinho, Caffarena, Lima, Capitaneo, & Ogasawara 2005). It is reported that iron nanoparticles was embedded in poly (methylmethacylate) with using melt-blending technique. The H_c values were the same for both % iron particles additions, about 260 Oe.

In this study magnetic polymer nano composites reinforced with barium hexaferrite were studied. Brabender has been used for mixing both powders and polymer. After that the mixing unshaped composites need some proceesses. Hot press was applied at 5.5 MPa in air. The reason for choosing barium hexaferrite is that in many studies barium hexaferrite has been used as a magnetic ceramic material. It is anisotropic and has a larger intrisintic magnetocrystalline anisotropy field. Due to the property of their in-plane anisotropy, it is easy to use these materials as a frequency absorber. The reason for choosing PVC is its economicy, easy to find, being a thermoplastic polymer as it is easy to shape the composite.

Here is the aim of this thesis:

1) To obtain the required phases for barium hexaferrite and to have hexagonal grain structure for barium hexaferrite powders.

2) To obtain polymer nanocomposites, that barium hexaferrite powders are highly dispersed into the polymer.

3) To obtain good magnetic properties for both barium hexaferrite powders and polymer nanocomposites for radar absorbing applications.

CHAPTER TWO
MAGNETISM AND MAGNETIC CERAMICS

Ceramic magnets have become firmly established as electrical and electronic engineering materials; most contain iron as a major constituent and are known collectively as 'ferrites'. From the point of view of electrical properties they are semiconductors or insulators, in contrast to metallic magnetic materials which are electrical conductors. One consequence of this is that the eddy currents produced by the alternating magnetic fields which many devices generate are limited in ferrites by their high intrinsic resistivities. To keep eddy currents to a minimum becomes of paramount importance as the operating frequency increases and this has led to the widespread introduction of ferrites for high-frequency inductor and transformer cores for example. Laminated metal cores are most widely used for low-frequency transformers. This single example illustrates how metal and ceramic magnetic materials complement each other; often it is physical properties which determine choice, but sometimes it is cost. Ferrites dominate the scene for microwave applications, and the transparency required for magneto-optical and radar absorbing applications is offered only by them. Ferrites have also become firmly established as the 'hard' (or permanent) magnet materials used for high-fidelity speakers and small electric motors (Moulson & Herbert, 2003).

2.1 Magnetic Ceramics: Basic Concepts

2.1.1 Origins of Magnetism in Materials

Ampere, Biot, Savart and Oersted were among the first to demonstrate that conductors carrying currents produced magnetic fields and exerted 'Lorentz' forces on each other. They were also responsible for determining the laws governing the magnetic fields set up by currents. It was established that a small coil carrying a current behaved like a bar magnet, i.e. as a magnetic dipole with magnetic moment μ (Fig. 2.1), and this led Ampe`re to suggest that the origin of the magnetic effect in materials lies in small circulating currents associated with each atom. These so-called

amperian currents each possess a magnetic moment ($\mu = IA$), and the total moment of the material is the vector sum of all individual moments. The amperian currents are now identified with the motion of electrons in the atom.
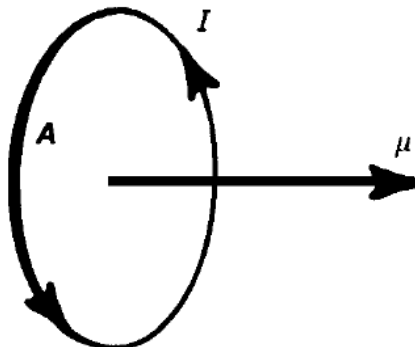
Figure 2.1 The magnetic moment of a current loop

(Moulson & Herbert, 2003)

2.1.2 Magnezation in matter from the macroscopic viewpoint

The field vector determining the Lorentz force on a current is the magnetic induction B, which is measured in teslas. In principle, B at a point P can be calculated for any system of currents in vacuo by the vector summation of induction elements dB, arising from current elements Idl (Figure 2.2), where

$$dB = \frac{\mu_0}{4\pi}\left(\frac{Idl \times r}{r^3}\right)$$

(2.1)

(μ_0 = permeability of a vacuum).

An additional field vector, the magnetic field intensity H measured in amperes per metre, is defined so that in a vacuum $H = B/\mu_0$. Therefore, whereas B depends upon the medium surrounding the wire (a vacuum in the present case), H depends only upon the current.

An important relation between D, E and P was derived by considering the effects of polarization in the dielectric of a parallel-plate capacitor. An analogous relationship is now derived by considering the magnetization of a material of a

wound toroid of cross-section A and mean circumference *l* (Figure 2.3(a)). Because there is no break in the toroid, and so no free poles and consequent demagnetizing fields, *H* in the material must be due to the real currents only. The material becomes magnetized, i.e. it acquires a magnetic moment per unit volume or magnetization *M*. Volume magnetic susceptibility is given below;

$$B = \mu_0 \left(1 + \chi_m \right) H = \mu_0 \mu_r H \qquad (2.2)$$

where, B: magnetic induction, μ: permeability, H: magnetic field intensity, λ_m: volume magnetic susceptibility (Moulson & Herbert, 2003).
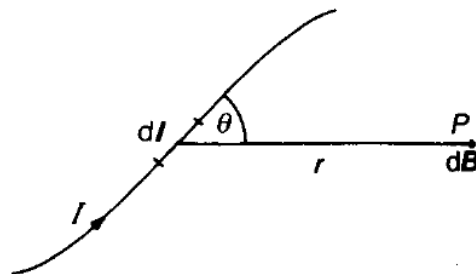
Figure 2.2 Magnetic induction arising from a current element (Moulson & Herbert, 2003)
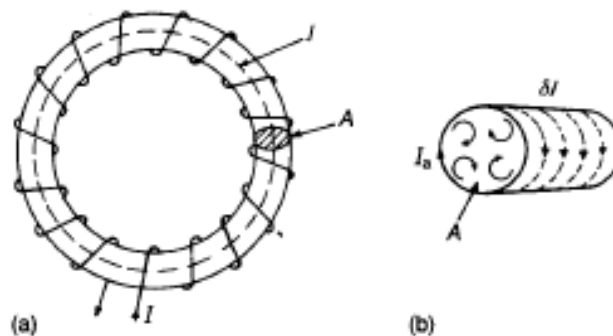
Figure 2.3. Effects arising from the presence of a magnetic magnetics (Moulson & Herbert, 2003)

2.1.3 Shape Anisptropy: Demagnetization

Measurements of permeability and associated magnetic properties are usually made on toroids of uniform section when, to a close approximation, the flux density *B* is uniform throughout the material and lies entirely within it. In most practical

applications the magnetic circuit is more complex, and variations in component section and permeability give rise to variations in flux density. Important effects arise from air gaps, which may be intentionally introduced or may be cracks or porosity.

The effect of the shape of a specimen on its magnetic behaviour, 'shape anisotropy', is expressed by a demagnetization factor N_D. A field H_a applied to a solid of arbitrary shape is reduced by a factor proportional to its magnetization M, so that the effective field H_e within the body is given by

$$H_e = H_a - N_D M \tag{2.3}$$
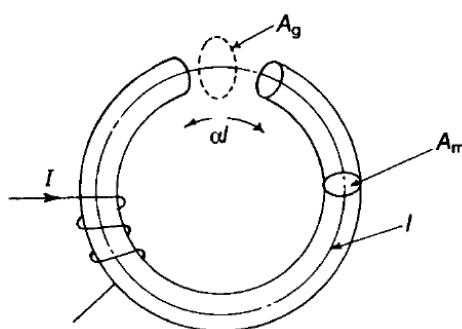
Figure 2.4 The effect of an air gap in a toroid

(Moulson & Herbert, 2003)

A thin flat disc magnetized normally to its plane will have a demagnetization factor close to unity so that its real permeability must be very high if its effective permeability is to be appreciable. Minor structural defects, such as fine cracks normal to the direction of magnetization, set up demagnetizing fields which can also markedly reduce effective permeability. The effect of such a crack can be calculated by considering a toroid of overall length l containing an air gap of length al, as shown in Figure 2.4; al is assumed to be very small so that the effective cross-section A_g of the gap, is approximately equal to the cross-section A_m of the toroid.

2.1.4 Classification of Magnetic Materials

There are various types of magnetic material classified by their magnetic susceptibilities χ_m. Most materials are *diamagnetic* and have very small negative susceptibilities (about 10^{-6}). Examples are the inert gases, hydrogen, many metals,

most non-metals and many organic compounds. In these instances the electron motions are such that they produce zero net magnetic moment. When a magnetic field is applied to a diamagnetic substance the electron motions are modified and a small net magnetization is induced in a sense opposing the applied field. As already mentioned, the effect is very small and of no practical significance in the present context, and is therefore disregarded.

Paramagnetics are those materials in which the atoms have a permanent magnetic moment arising from spinning and orbiting electrons. An applied field tends to orient the moments and so a resultant is induced in the same sense as that of the applied field. The susceptibilities are therefore positive but again small, usually in the range 10^{-3}–10^{-6}. An important feature of many paramagnetics is that they obey Curie's law $\chi_m \propto 1/T$, reflecting the ordering effect of the applied field opposed by the disordering effect of thermal energy. The most strongly paramagnetic substances are compounds containing transition metal or rare earth ions and ferromagnetics and ferrites above their Curie temperatures.

Ferromagnetic materials are spontaneously magnetized below a temperature termed the Curie point or Curie temperature. The spontaneous magnetization is not apparent in materials which have not been exposed to an external field because of the formation of small volumes (domains) of material each having its own direction of magnetization. In their lowest energy state the domains are so arranged that their magnetizations cancel. When a field is applied the domains in which the magnetization is more nearly parallel to the field grow at the expense of those with more nearly antiparallel magnetizations. Since the spontaneous magnetization may be several orders of magnitude greater than the applied field, ferromagnetic materials have very high permeabilities. When the applied field is removed some part of the induced domain alignment remains so that the body is now a 'magnet' in the ordinary sense of the term.

Spontaneous magnetization is due to the alignment of uncompensated electron spins by the strong quantum-mechanical 'exchange' forces. It is a relatively rare phenomenon confined to the elements iron, cobalt, nickel and gadolinium and certain

alloys. One or two ferromagnetic oxides are known, in particular CrO_2 which is used in recording tapes. These ferromagnetic oxides show metallic-type conduction and the mechanism underlying their magnetic behaviour is probably similar to that of magnetic metals.

In *antiferromagnetic* materials the uncompensated electron spins associated with neighbouring cations orient themselves, below a temperature known as the Néel point, in such a way that their magnetizations neutralize one another so that the overall magnetization is zero. Metallic manganese and chromium and many transition metal oxides belong to this class. Their susceptibilities are low (about 10^{-3}) except when the temperature is close to the Néel point when the antiferromagnetic coupling breaks down and the materials become paramagnetic.

Finally, there are the important *ferrimagnetic* materials, the subject of much of this text. In these there is antiferromagnetic coupling between cations occupying crystallographically different sites, and the magnetization of one sublattice is antiparallel to that of another sublattice. Because the two magnetizations are of unequal strength there is a net spontaneous magnetization. As the temperature is increased from 0 K the magnetization decreases.

2.1.5 Magnetostriction

Because of the spin–orbit lattice coupling referred to in the previous section, changes in the spin directions result in changes in the orientation of the orbits which, because they are restrained by the lattice, have the effect of slightly altering the lattice dimensions. This effect is known as magnetostriction.

The magnetostriction constant λ_m is defined as the strain induced by a saturating field; it is given a positive sign if the field causes an increase in dimensions in the field direction. For single crystals λ_m varies with the crystallographic direction, and so for the ceramic form it is an average of the single-crystal values. λ_m values for some polycrystalline ferrites are given in Table 2.1.

Table 2.1 Saturation magnetostriction constants for some
polycrstalline ferrites (Moulson & Herbert, 2003)

Composition	$\lambda_{\mathrm{m}}/10^{-6}$
Fe_3O_4	$+40$
$MnFe_2O_4$	-5
$CoFe_2O_4$	-110
$NiFe_2O_4$	-26
$Ni_{0.56}Fe_{0.44}^{2+}Fe_2O_4$	0
$Ni_{0.5}Zn_{0.5}Fe_2O_4$	-11
$MgFe_2O_4$	-6
$TbFe_2$ a 'giant' magnetostrictor	$> 10^3*$

2.1.6 Weiss Domains

The fact that spontaneous magnetization exists in, for example, a piece of iron, and yet the overall magnetization can be zero, is explained by the existence of domains. Below its Curie temperature a ferromagnetic or ferromagnetic body consists of a large number of small domains, each spontaneously magnetized to saturation. Each grain or crystallite in a polycrystalline magnetic ceramic may contain a number of domains, each differing from its neigbour only in the direction of magnetization.

A single crystal with uniform magnetization, i.e. a single-domain single crystal, has magnetostatic energy due to the external magnetic field which it generates. If the crystal is divided into oppositely oriented parallel domains, the energy will be greatly reduced since the flux can now pass from one to another of the closely adjacent domains (Figure 2.5(a)). In cubic materials, such as spinels and garnets, zero magnetostatic energies are possible through the formation of closure domains (Figure 2.5(b)) since the external flux is now close to zero. Even so, the system has magnetoelastic energy because magnetostriction leads to straining between the long and the triangular domains (Moulson & Herbert, 2003).

The boundary between two adjacent domains is known as a domain wall or Bloch wall. A Bloch wall is the region between two domains in which the elementary spin

moments change smoothly from one orientation to another. For example, in the case of the anti-parallel domains the change in direction of the vectors in moving from one domain to an adjacent one would be as shown diagrammatically in Figure 2.6.
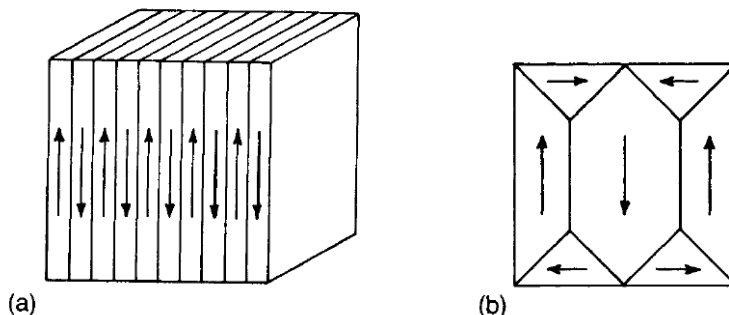
Figure 2.5 Idealized magnetic domain configurations: (a) antiparalleldomains;

(b) flux closure domains (Moulson & Herbert, 2003)
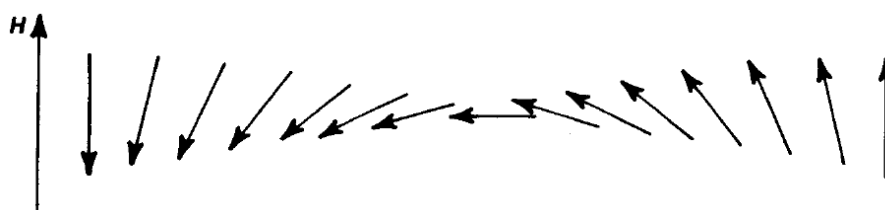
Figure 2.6 The change in spin orientation across the width of a Bloch Wall

(Moulson & Herbert, 2003)

2.1.7 Magnetization in a Multidomain Crystal

The most characteristic feature of ferromagnetic or ferrimagnetic materials are the relationship between *B* and *H* (Figure 2.7). The line deOba – the 'virgin curve' – represents the relationship determined experimentally when the specimen is demagnetized before each measurement of the induction for a given field. The change in *B*, very near to the origin, represents magnetization by reversible Bloch wall displacements, and the tangent OC to this initial magnetization curve is called the initial permeability μ_i. The steep rise in *B* represents magnetization by irreversible Bloch wall displacements as the walls break away from their pinning points, and the region ba represents magnetization by reversible and irreversible domain rotations from one easy direction to another more favourably aligned with

the applied field. The latter process requires high field strengths because the magnetization within a domain is rotated against the anisotropy field.
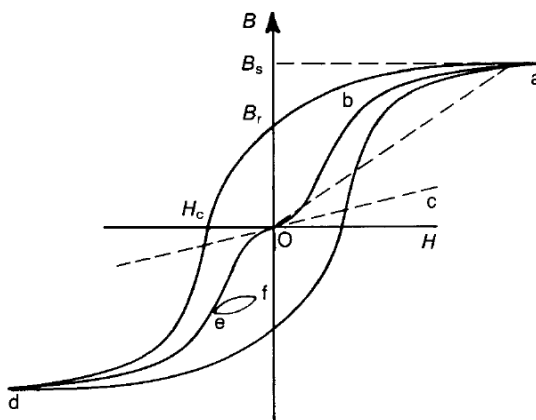
Figure 2.7 Magnetic B-H hystresis loop

(Moulson & Herbert, 2003)

The slope of Oa, from the origin to the tip of the loop, gives the amplitude permeability μ_a which has a maximum value when the peak field corresponds to the point b on the virgin curve. If a relatively small alternating field is superimposed on a static field, a minor loop such as ef is obtained, and the amplitude permeability of this is known as the incremental permeability μ_Δ. As far as applications are concerned, μ_i is important for inductors where only small alternating fields are encountered, μ_a is important for power transformers when large alternating fields are involved and μ_Δ is important for transductors to which both alternating and static fields are applied.

If, after the material has been magnetically saturated to the value B_s, the field is reduced to zero, the magnetization vectors rotate out of line with the field towards the nearest preferred direction which is determined in part by magnetocrystalline anisotropy. The magnetization is thus prevented from complete relaxation to the 'virgin' curve and hence, for zero field, there is a remanent induction B_r. In order to reduce the induction to zero a reverse field H_c has to be applied. The coercive field or 'coercivity' H_c depends in part on crystalline anisotropy, as might be expected.

Because of hysteresis, energy is dissipated as heat in a magnetic material as it is taken round a complete *B–H* loop, and the hysteresis energy loss W_h per unit volume of material is

$$W_h = \oint BdH \qquad\qquad (2.4)$$

Magnetic materials are usually characterized as 'hard' or 'soft', depending on the magnitude of their coercivities (Figure 2.8) (Moulson & Herbert, 2003).
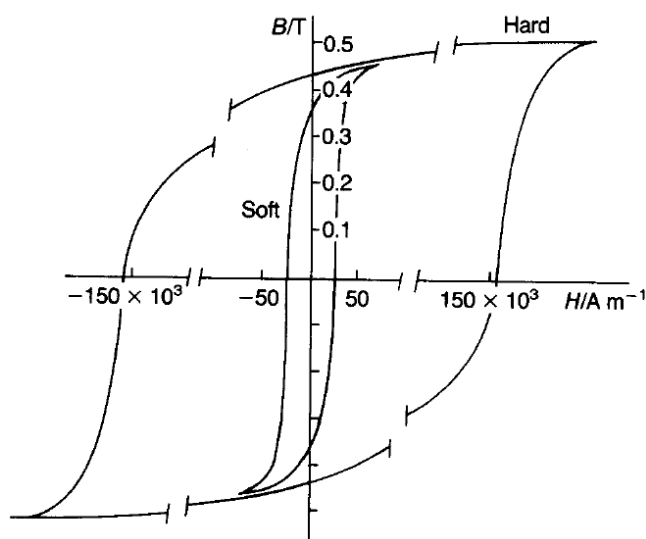
Figure 2.8 Hysteresis loops illustrating the distinction between magnetically 'soft' and 'hard' (Moulson & Herbert, 2003)

2.2. Model Ferrites

2.2.1 Spinel Ferrites: Model NiOFe₂O₃

Magnetite (Fe_3O_4), a naturally occurring ferrite, is the earliest known magnetic material. Its composition can be written $FeOFe_2O_3$, when the structural relationship to the mineral spinel ($MgOAl_2O_3$) is apparent. There are many other possible compositions with the general formula $MeOFe_2O_3$, in which Me represents a divalent ion such as Mn^{2+}, Fe^{2+}, Co^{2+}, Ni^{2+}, Cu^{2+} or Zn^{2+}, or a combination of divalent ions with an average valence of 2.

In the spinel crystal structure the oxygen ions form a cubic close-packed array in which, two types of interstice occur, one coordinated tetrahedrally and the other octahedrally with oxygen ions. The cubic unit cell is large, comprising eight formula units and containing 64 tetrahedral and 32 octahedral sites, customarily designated A and B sites respectively; eight of the A sites and 16 of the B sites are occupied. The unit cell shown in Figure 2.9 is seen to be made up of octants, four containing one type of structure (shaded) and four containing another (unshaded). In this representation some of the A-site cations lie at the corners and face-centre positions of the large cube; a tetrahedral and an octahedral site are shown. The close-packed layers of the oxygen ion lattice lie at right angles to the body diagonals of the cube. The arrows on the ions, representing directions of magnetic moments, indicate that the B-site ions have their moments directed antiparallel to those of A-site ions, illustrating the antiferromagnetic coupling.
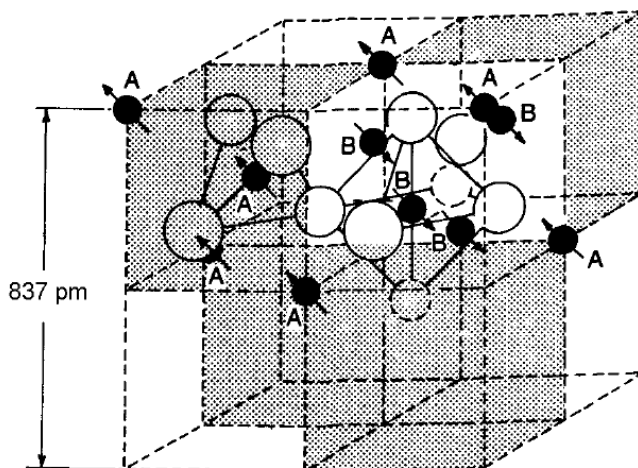
Figure 2.9 The unit cell of a magnetic inverse spinel

(Moulson & Herbert, 2003)
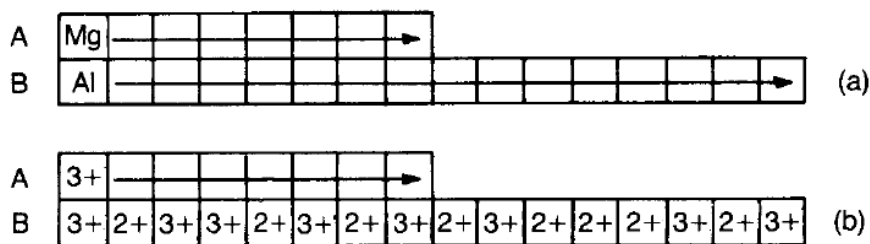
Figure 2.10 Diagrammatic Represantation of site occupancy in (a) normal and (b) inverse spinels (Moulson & Herbert, 2003)

The occupancy of sites in the spinel-type minerals is conveniently represented with the help of the diagrams in Figure 2.10. In the case of the mineral spinel the divalent ions (Mg) occupy the A sites and the trivalent ions (Al) the B sites (Figure 2.10(a)). This is known as the normal spinel structure. In the spinel ferrites ($MeFe_2O_4$) different ions exhibit different site preferences. In nickel ferrite, for instance, the Ni^{2+} ions occupy B sites along with an equal number of randomly distributed Fe^{3+} ions, whilst the remaining Fe^{3+} ions occupy A sites. This is termed an inverse spinel structure (Figure 2.10(b)). Figure 2.11 shows saturation magnetization per "formula unit" for the ferrite $(Fe^{3+}_{1-\delta}Zn^{2+}_{\delta})(Fe^{3+}_{1+\delta}Ni^{2+}_{1-\delta})O_4$ as a function of δ (Moulson & Herbert, 2003).
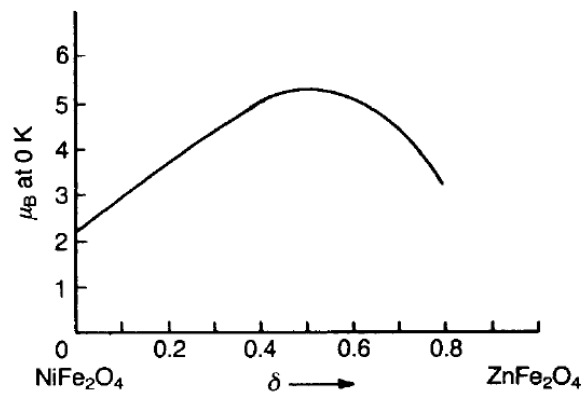
Figure 2.11 Saturation magnetization per 'formula Unit for the ferrite $(Fe^{3+}_{1-\delta}Zn^{2+}_{\delta})(Fe^{3+}_{1+\delta}Ni^{2+}_{1-\delta})O_4$ as a functaion (Moulson & Herbert, 2003)

2.2.2 Hexaferrites: Model $BaFe_{12}O_{19}$

Barium hexaferrite ($BaFe_{12}O_{19}$) is the model for a family of 'M-type ferrites', so called because they are based upon the hexagonal magnetoplumbite, or M structure. Its crystal structure, though related to that of the spinels, is very much more complex. The large unit cell (c = 2.32 nm; a = 0.588 nm) contains two formula units, i.e. a total of 64 ions. The Ba^{2+} and O^{2+} ions together form a close-packed structure with some of the layers cubic close-packed and others hexagonal close-packed. The origins of the magnetic properties are basically the same as those already discussed and can be summarized as follows: of the 12 Fe^{3+} ions in a formula unit, nine are on octahedral sites two on tetrahedral sites and one on a five-coordinated site; seven of the ions on octahedral sites and the one on a five-coordinated site have their spins in one sense,

and the remainder are oppositely directed. Thus there are four more ions with spins in the one sense than there are with spins in the other and, since there are five electrons with parallel spins in each Fe^{3+} ion, there are 20 unpaired spins per formula unit, leading to a saturation magnetization of 20 μ_B per cell volume. $BaFe_{12}O_{19}$ has a high magnetic anisotropy with its 'prefered direction of magnetization' ('easy' direction) along the c-axis. Various substitutions are made to tailor intrinsic magnetic properties, for example Sr for Ba, and partial substitution of Al for Fe to increase coercivity (Moulson & Herbert, 2003).

2.2.3 Garnets: models $Y_3Fe_5O_{12}$ (YIG)

'Garnet' is the name of a group of isostructural minerals with the general composition $3R'O.R_2''O_3.3SiO_2$. Examples are $3CaO.Al_2O_3.3SiO_2$ (grossularite), $3CaO.Fe_2O_3.3SiO_2$ (andradite) and $3MnO.Al_2O_3.3SiO_2$ (spessarite). Yttrium iron garnet (YIG) is the best known of a family of ferromagnetic garnets because of its importance as a microwave material.

The general formula for the for the ferrimagnetic garnets is written $R_3Fe_5O_{12}$, where R stands for yttrium in the case of YIG; the yttrium can be totally or partially replaced by one of the lanthanides such as lanthanum, cerium, neodymium, gadolinium etc.
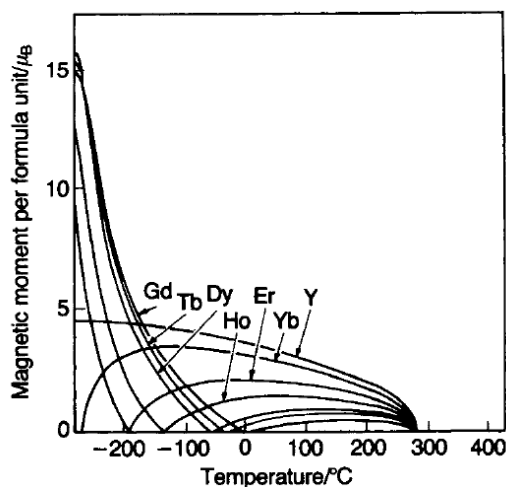
Figure 2.12 Variation of saturation magnetization
with temperature for various garnets
(Moulson & Herbert, 2003)
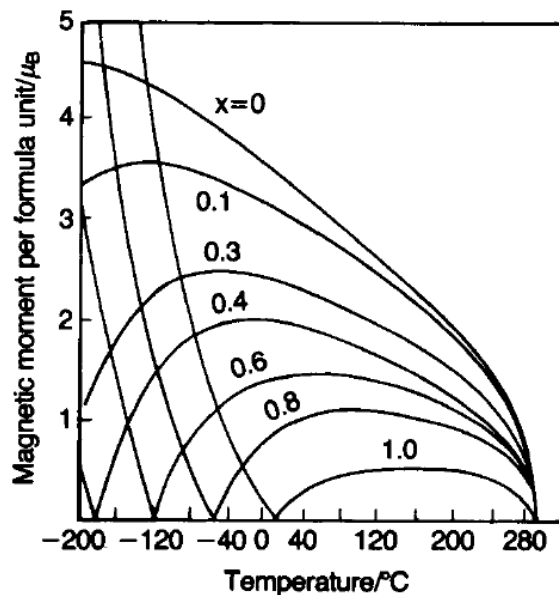
Figure 2.13 Variation of saturation magnetization

with temperature for $Y_{3(1-x)}Gd_{3x}Fe_5O_{12}$

(Moulson & Herbert, 2003)

The types of saturation magnetization–temperature characteristic for the various garnet ferrites are summarized in Figure 2.12. Figure 2.13 illustrates for a series of the yttrium gadolinium iron garnets an important feature associated with a compensation point which is exploited in certain applications: the magnetization can be arranged to be almost independent of temperature over a chosen temperature range. For example, for the composition corresponding to x=0.6, i.e. $Y_{1.2}Gd_{1.8}Fe_5O_{12}$, the saturation magnetization is relatively stable over a wide temperature range centred around 50°C (Moulson & Herbert, 2003).

2.3 Properties Influencing Magnetic Behaviour

2.3.1 Soft Ferrites

Soft ferrites are used for the manufacture of inductor cores (pot cores) for telecommunications, low-power transformers, and as television tube scanning yokes (Figure 2.14). The more important material characteristics for these and other applications are now discussed with emphasis on the influence of composition and microstructure.

Figure 2.14 Range of soft ferrite components: (i) TV scanning yoke (components kindly
supplied by Philips Components Ltd.); (ii) UR core and TV line output transformer;
(iii) E core for switched mode power supply; (iv) wide band transformer core; (v) core
giving good magnetic shielding; (vi) high Q (adjustable) filter core (cf. Fig. 9.48);
(vii) precision ferrite antenna for transponder; (viii) multilayer EMI suppressors;
(ix) toroids for laser and radar pulse applications; (x) typical EMI
shields for cables. ((ii)–(x) Courtesy of 'Ferroxcube UK'.)
(Moulson & Herbert, 2003)

2.3.1.1 Initial Permeability (μ_{ri})

High initial permeability is achieved through control of composition and microstructure. It depends in a complex manner on high saturation magnetization, low magnetic anisotropy and low magnetostriction. The magnetic anisotropy falls off very rapidly as the saturation magnetization falls to a low value near the Curie temperature, so that the net result is a peak in permeability just below the Curie temperature followed by a steep fall to a value close to unity as the magnetization falls to zero. Figure 2.15 shows the variation of the initial relative permeability, μ_{ri}, with temperature for different δ values in $Mn_{1-\delta}Zn_{\delta}Fe_2O_4$ and $Ni_{1-\delta}Zn_{\delta}Fe_2O_4$.

Magnetostriction can be reduced by adjusting the sintering atmosphere during the application of the maximum temperature and afterwards so that a small amount of Fe^{2+} is formed, thus taking advantage of the opposite sign of the magnetostriction constant for Fe_3O_4 compared with that for most other ferrites.
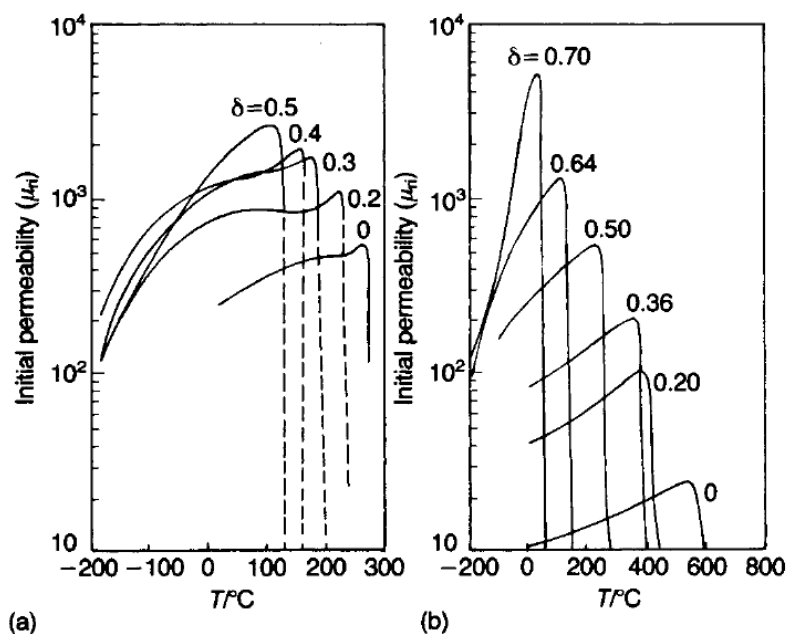
Figure 2.15 The variation with temperature of the initial relative permeability μ_{ri} for different δ values in (a) $Mn_{1-\delta}Zn_{\delta}Fe_2O_4$ and (b) $Ni_{1-\delta}Zn_{\delta}Fe_2O_4$ (Moulson & Herbert, 2003)

Because a major contribution to μ_{ri} is from Bloch wall movements, microstructure has a significant influence. High magnetic anisotropy implies high-energy walls readily 'pinned' by microstructural defects. Thus, for a high-permeability polycrystalline ferrite, very mobile domain walls are required, demanding in turn large defect-free grains coupled with low magnetic anisotropy. Figures 2.16 and 2.17 illustrate the sensitivity of permeability to grain size, and Figure 2.18 shows how porosity leads to reduced permeability, presumably because of domain wall pinning.
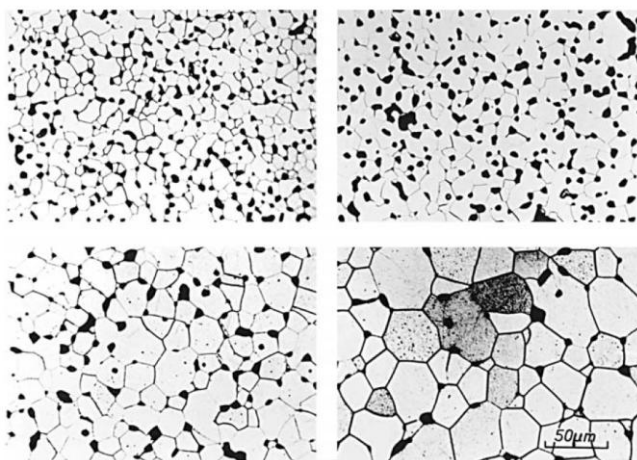
Figure 2.16 Microstructure of high permeability Mn-Zn ferrites with a range of grain sizes: (a) $\mu_{ri} = 6500$; (b) $\mu_{ri} = 10000$; (c) $\mu_{ri} = 16000$; (d) $\mu_{ri} = 21500$ (Moulson & Herbert, 2003)
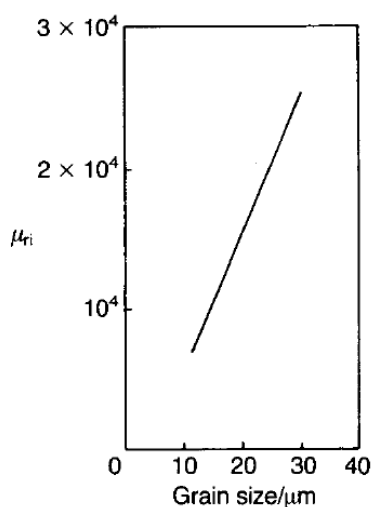
Figure 2.17 Dependence of the initial relative permeability on grain size (Moulson & Herbert, 2003)
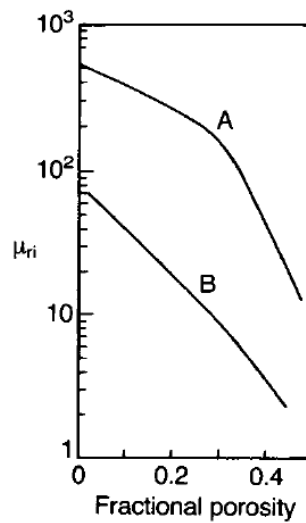
Figure 2.18 Dependence of
the initial relative permeability
on porosity: curve A,
$Ni_{0.5}Zn_{0.5}Fe_2O_4$; curve B, $NiFe_2O_4$
(Moulson & Herbert, 2003)

2.3.1.2 The loss factor (tanδ)/μ_{ri}

The way in which magnetic loss in a material is expressed depends upon the particular application to which the component made from the material is put.

2.3.1.3 Electrical resistivity

The resistivity ρ of an inductor core material is important because it determines eddy current losses. In general room temperature resistivities of ferrites lie in the range 10^{-1}-10^6 Ωm. Typical resistivity–temperature data for MnZn and NiZn ferrites are shown in Figure 2.19. For both types the conductivity mechanism is believed to be electron hopping between ions of the same type on equivalent lattice sites, e.g. $Fe^{3+}\leftrightarrow Fe^{2+}$, $Mn^{3+}\leftrightarrow Mn^{2+}$ or $Ni^{3+}\leftrightarrow Ni^{2+}$.
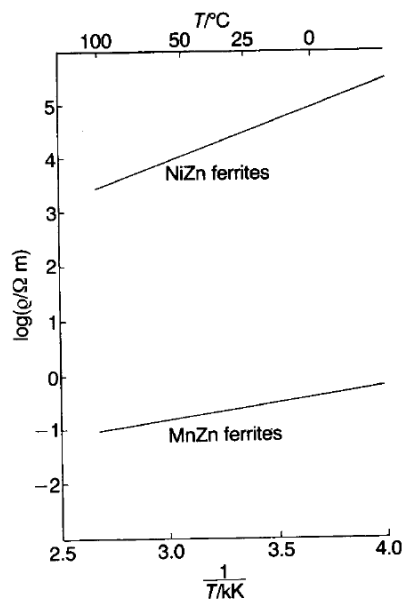
Figure 2.19 Temperature dependence

of the resistivity for NiZn and MnZn

and MnZn ferrites

(Moulson & Herbert, 2003)
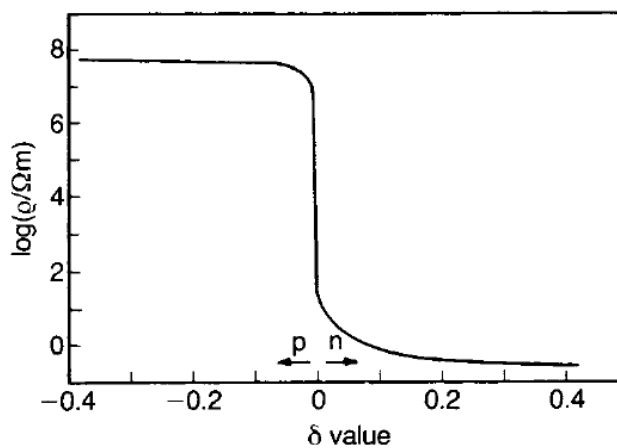
Figure 2.20 Dependence of the ferrite $Ni_{0.23}Zn_{0.7}Fe_{2+\delta}O_{4-x}$

on the iron content (Moulson & Herbert, 2003)

Fig. 2.20 shows electrical resistivity data for $Ni_{0.23}Zn_{0.7}Fe_{2+\delta}O_{4-x}$ in which δ measures the amount of iron (Moulson & Herbert, 2003).

2.3.1.4 Permittivity

Above a frequency of 1GHz the permittivity of MnZn ferrites is around 10, but at 1 kHz it can reach values in the range 10^4–10^6. Figure 2.21 shows the frequency dispersion of ε_r and the dielectric loss tangent for the ferrite $Ni_{0.4}Zn_{0.6}Fe_2O_4$.
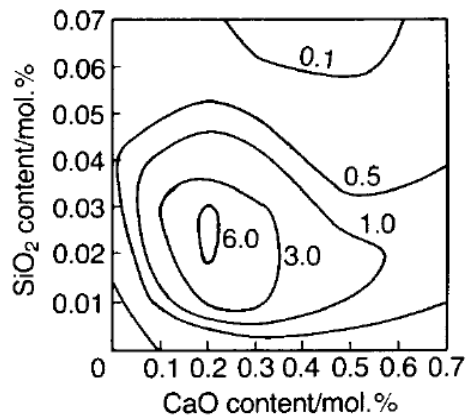
(a)
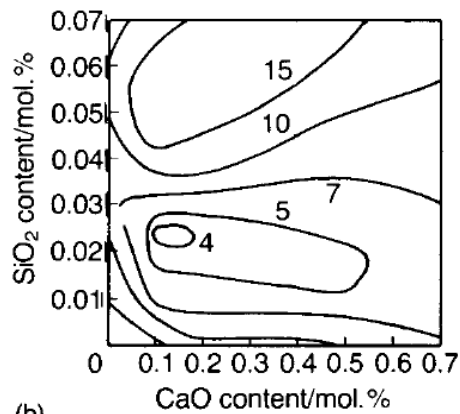
(b)

Figure 2.21 Influence of SiO_2 and CaO additions to the ferrite $Mn_{0.68}Zn_{0.2}Fe_2O_4$ on (a) resistivity (Ωm) and loss factor ((tan δ)/μ'_{ri} x 10^{-6}) at 100 kHz (Moulson & Herbert, 2003)

2.3.1.5 Resonance Effects

Figure 2.22 shows magnetic properties of $Ni_{1-\delta}Zn_\delta Fe_2O_4$ as functions of δ and frequency.
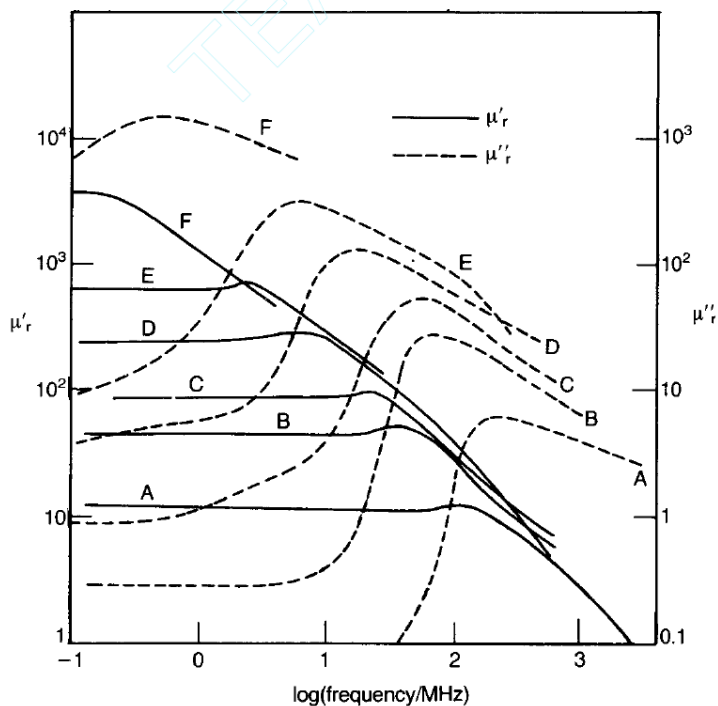
Figure 2.22 Magnetic properties of polycrystalline $Ni_{1-\delta}Zn_\delta Fe_2O_4$
as functions of δ and frequency; curve A, $\delta = 0$; curve B, $\delta = 0.2$;
curve C, $\delta = 0.36$; curve D, $\delta = 0.5$; curve E, $\delta = 0.64$; F, $\delta = 0.7$
(Moulson & Herbert, 2003)

2.3.2 Hard Ferrites

Permanent magnetic materials are distinguished from the 'soft' variety by their high coercivity H_c, typically above 150 kAm^{-1}. There are various parameters;

2.3.2.1 Remanence (B_r)

Remanence is determined partly by the saturation magnetization M_s and partly by the extent to which domain development disorients the magnetization vectors on

removal of the saturating field. Figure 2.23 shows microstructure of an oriented barium hexaferrite. Figure 2.24 shows demagnetization curves for an oriented barium hexaferrite and an oriented hexaferrite.

Figure 2.23 Microstructure of an oriented

barium hexaferrite

(Moulson & Herbert, 2003)
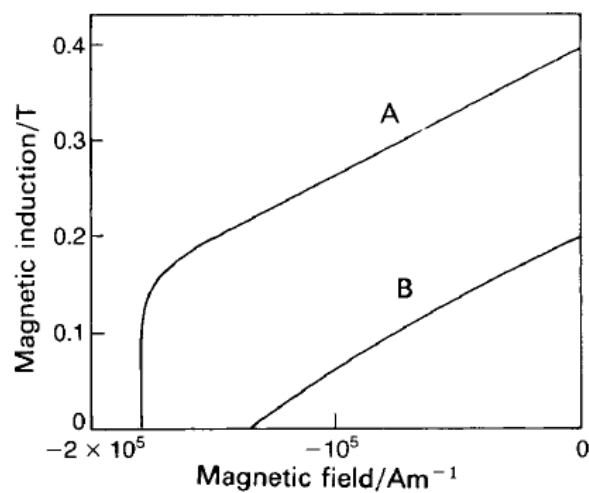
Figure 2.24 Demagnetization curves for an oriented

barium hexaferrite (curve A) and an isotropic

hexaferrite (curve B)

(Moulson & Herbert, 2003)

2.3.2.2 Coersivity (H_c)

The high coercivity of the hexaferrites depends basically on their high magneto-crystalline anisotropy which results in anisotropy fields of approximately 1400 kAm^{-1}. Figure 2.25 shows the dependence of coercivity on the particle size of a barium hexaferrite powder (Moulson & Herbert, 2003).
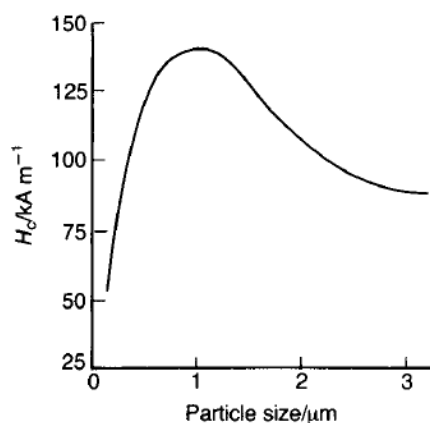
Figure 2.25 The dependence of corecivity
on the particle size of a barium hexaferrite
powder (Moulson & Herbert, 2003)

2.4 Preparation of Ferrites

2.4.1 Raw Materials

The raw materials can be minerals that have only been purified by mechanical methods or the purer products of chemical processes. Both hematite (Fe_2O_3) and magnetite (Fe_3O_4) occur in large deposits of better than 90% purity that, for some ferrites, require little more than grinding before use. A purer grade of Fe_2O_3 can be obtained from the pickle liquor that results from the removal of oxide crusts during steel fabrication.

2.4.2 Mixing, calcining and milling

Mixing is usually carried out in a ceramic ball mill with steel balls. The inevitable attrition of the mill balls leads to an addition of 0.5–1 wt% to the iron content for which allowance must be made. Care must be taken to maintain the quantity and size

distribution of the mill balls and to remove those that have become so small that they cannot be separated from the slip or powder on sieving.

Calcination (typically at temperatures in the range 1000–1100°C, depending on composition) is carried out in saggars or continuously in a rotating tube kiln. An air atmosphere is used even though this results in a high Mn^{3+} content in MnZn ferrites, but the state of oxidation is rapidly rectified during sintering. A low Mn^{3+} content can be a disadvantage during the early stages of sintering since, at about 430°C, MnZn ferrites take up oxygen, converting Mn^{2+} to Mn^{3+} with resulting lattice shrinkage. The temperature gradients within a furnace are often considerable at this stage in firing and the pressings are weak. One part of a large piece may be shrinking while another part is expanding, resulting in the formation of cracks. At temperatures above 700°C the thermal gradients are greatly reduced because of the rapid interchange of radiant energy so that effects of this type are less likely to cause problems (Moulson & Herbert, 2003).

2.4.3 Sintering

If a low oxygen pressure is required during sintering nitrogen is injected at a point in the tunnel kiln where the temperature is approximately 1000°C, and the air is effectively displaced at a position where the temperature is 1300°C. The composition of the atmosphere is monitored by passing samples from the hot zone through a paramagnetic oxygen meter or by using a zirconia solid state electrolytic device within the furnace. The low oxygen pressure (around 1 kPa (7.5 Torr)) is maintained until the pieces have cooled to around 500°C. A controlled atmosphere can also be obtained by burning methane or town gas in a limited supply of air. The large-scale process in a continuous kiln does not allow full atmosphere control because the extent to which oxygen gains access to the hot zone is governed by so many variables, one of which is the packing of the work on the trolleys which inevitably varies with the sizes and shapes of the pieces concerned. Where close control is essential, as with pot cores, the pieces are fired in well sealed batch kilns. In this case the oxygen pressure can be programmed to correspond to the equilibrium pressure of

the desired balance of oxidation states at both the maximum temperature and as it falls to around 900°C. Below 900°C the rate at which oxygen is exchanged between the ferrite and the atmosphere is sufficiently slow that, provided that the cooling is rapid, there is no need to maintain tight control. Means are often provided for moving the sintered material into a cooled compartment when the temperature has fallen sufficiently.

In the cases of $NiFe_2O_4$ and the rare earth garnets for microwave use, in which the losses due to conductivity must be minimized, an oxygen atmosphere may be required for sintering so that the concentration of Fe^{2+} ions is reduced to a very low level (Moulson & Herbert, 2003).

2.4.4 Single-crystal ferrites

They are used in the read-out heads of tape recorders, which must be highly abrasion resistant. MnZn ferrite crystals of sufficient size can be grown using the Bridgman–Stockbarger method. Garnet ferrite crystals are required for many microwave applications and as thin layers for bubble memories. For example gadolinium garnet crystals.

Magnets with oriented microstructures can be produced by using isostatic pressing and extrusion methods.

2.5 Applications

Ferrites are usually used in various applications such as;
- Inductors and transformers for small-signal applications
- Transformers for power applications
- Antennas
- Information storage
- Microwave devices
- Permanent magnets

Recently novel studies have been carried out about electromagnetic (EM) absorber materials due to the fact that electromagnetic absorber materials can be used various special areas such as electromagnetic interference shielding and reduction of radar cross section in military applications. Electromagnetic interference can cause device malfunctions, generating false images and reducing performance of electronic circuits. The reduction of radar cross section (RCS) is another important application of electromagnetic absorber materials. There are several methods to reduce RCS such as shaping the targets and employing radar absorbing material (RAM) or radar absorbing structure (RAS). The shaping process involves modifying the external features of the target to reduce the EM waves backscattered to the direction of radar source.

Barium hexaferrite powders have been investigated as a material for permanent magnets, microwave absorber devices and recording media. Barium hexaferrite is widely used due to its high stability, excellent high frequency response, narrow switching field distribution and the temperature coefficient of the coercivity in various applications. Barium ferrite with hexagonal molecular structure has fairly large magneto crystalline anisotropy, high Curie temperature and relatively large magnetization as well as chemical stability and corrosion stability.

Different methods were used to obtain good quality barium ferrite. A lot of studies were achieved to modify the magnetic parameters of barium ferrite by substituting. The preparation methods of barium ferrites affect their magnetic and structural properties. The sol-gel method has emerged as a new method for synthesizing barium ferrite for these applications. This method strongly determines their homogeneity, particle size, shape and magnetic characteristics (Dong et.al., 2006, Ghasemi et.al., 2007, Ghasemi, Saatchi, 2006, Ghasemi, Hossienpour, 2006).

CHAPTER THREE
PRODUCTION OF POLYMER NANOCOMPOSITES

This chapter covers the production of polymer nanocomposites especially focused on the magnetic polymer nanocomposites and gives details of preparation method of nano-sized particles.

3.1 Production Methods of Polymer Nanocomposites

Reinforcement of polymers with a second phase, whether inorganic or organic, to produce a polymer composite is common in the production of modern plastics. Polymer nanocomposites (polymer nanocompositess) represent a radical alternative to these conventional polymer composites and they are classified in several groups. Hence, application area has been focused on layered nanocomposites, production methods for the layered nanocomposites has developed and applied extensively. The classification of polymer nanocomposites can be divided into three main groups such as melt processing, solution induced intercalation and in situ polymerization.

3.1.1 In-Situ Polymerization

In-situ routes to polymer nanocomposites are the creation of the nanoelement within the polymer matrix by chemical means or chemical separation. The polymer matrix provides the template which the nanoelement is formed (Vaia, 2002) This method includes inserting a polymer precursor between layers and then expanding and dispersing the layers into the matrix by polymerization (Gao, 2004). Polymerization can be commenced either by heat or radiation, by the diffusion of a suitable initiator, by an organic initiator or catalyst fixed through cation exchange inside the interlayer before the monomer swelling step (Okamoto, 2005). One of the example of this route is the decomposition or chemical reaction of a precursor introduced to the polymer matrix (Vaia, 2002). The initial work in this area was carried out by the Toyota Research Group to produce clay/nylon-6 nanocomposites. This method is capable of producing well-exfoliated nanocomposites and has been

applied to a wide range of polymer systems. The technology is suitable for raw polymer manufacturers to produce clay/polymer nanocomposites in polymer synthetic processes and is also especially useful for thermosetting polymers (Gao, 2004).

3.1.2 Solution-induced intercalation

This method is based on a solvent system in which polymers or prepolymers are soluble and the silicate layers are swellable. In addition to this, method also applies solvents to swell first in a solvent such as water, chloroform or toluene etc. and disperse clays into a polymer solution. When the polymer and layered silicate solutions are mixed, the polymer chains intercalate together and displace the solvent within the interlayer of the silicate. After solvent removal, the intercalated structure remains resulting in PLS (polymer layered silicate) nanocomposites. This approach has difficulties for the commercial production of nanocomposites for most engineering polymers because of the high cost of the solvents required and the phase separation of the synthesized products from those solvents (Okamoto, 2005; Gao, 2004).

3.1.3 Melt Processing

This type of method induces the intercalation of clays and polymers during melting processing. Melt processing includes annealing, statically or under shear a mixture of the polymer organically modified layered silicats above the softening point of the polymer (Okamoto, 2005). The efficiency of intercalation using this method may not be as high as that of in situ polymerization and often the composites produced contain a partially exfoliated layered structure (Gao, 2004). However, there are some very important advantages of melt processing. Firstly, this method is environmentally benign due to the absence of organic solvents. Therefore, this is much preferred for practical industrial material due to its high efficiency and its possible avoidance of environmental hazards (Okamoto, 2005). Second, the approach can be applied by the polymer processing industry to produce nanocomposites based

on traditional polymer processing techniques, such as extrusion and injection (Gao, 2004).

In addition to these three major processing methods, other fabrication techniques have been also developed. These include solid intercalation, covulcanization, and the sol-gel method. Some of these methods are in the early stages of development and have not yet been widely applied.

3.2 Magnetic Polymer Nanocomposites

One of the main issue in preparing good polymer matrix nanocomposites samples is the good dispersion of the nanoparticles in a polymer matrix (Gupta et al., 2008). In addition to this, the performance of these materials is closely related to the dimensions of the magnetic component, the organization of the components, and the organic-inorganic synergies. Therefore, synthetic methods must be versatile, and they must guarantee a fine control of particle size, particle size dispersion, particle-polymer interactions and particle-polymer ordering. The starting point is a bulk material and it proceeds by mechanical attrition. This procedure consumes energy and yields high particle size dispersion, therefore its utility is quiet limited. Starting materials for the synthesis of magnetic composites are a monomer and a molecular precursor of the magnetic component. The basic processes for making a magnetic composite are the polymerization of the monomer, formation of the magnetic component (precipitation), and mixing of the magnetic and polymer components together. The process of making magnetic composites can be stepped as fallows and The four routes for the synthesis of magnetic nanocomposites are shown in Figure 3.1.

a) Seperated precipitation of the magnetic component and polymerization, and then mixing of the magnetic nanoparticles and the polymer

b) Precipitation of the magnetic component, mixing the nanoparticles with the monomer, and then in-situ polymerization;

c) Polymerization, mixing of the precursor with the polymer, and then in-situ precipitation;

d) Mixing monomer and precursor, and then simultaneous precipitation and polymerization. (Mai & Yu, 2006)
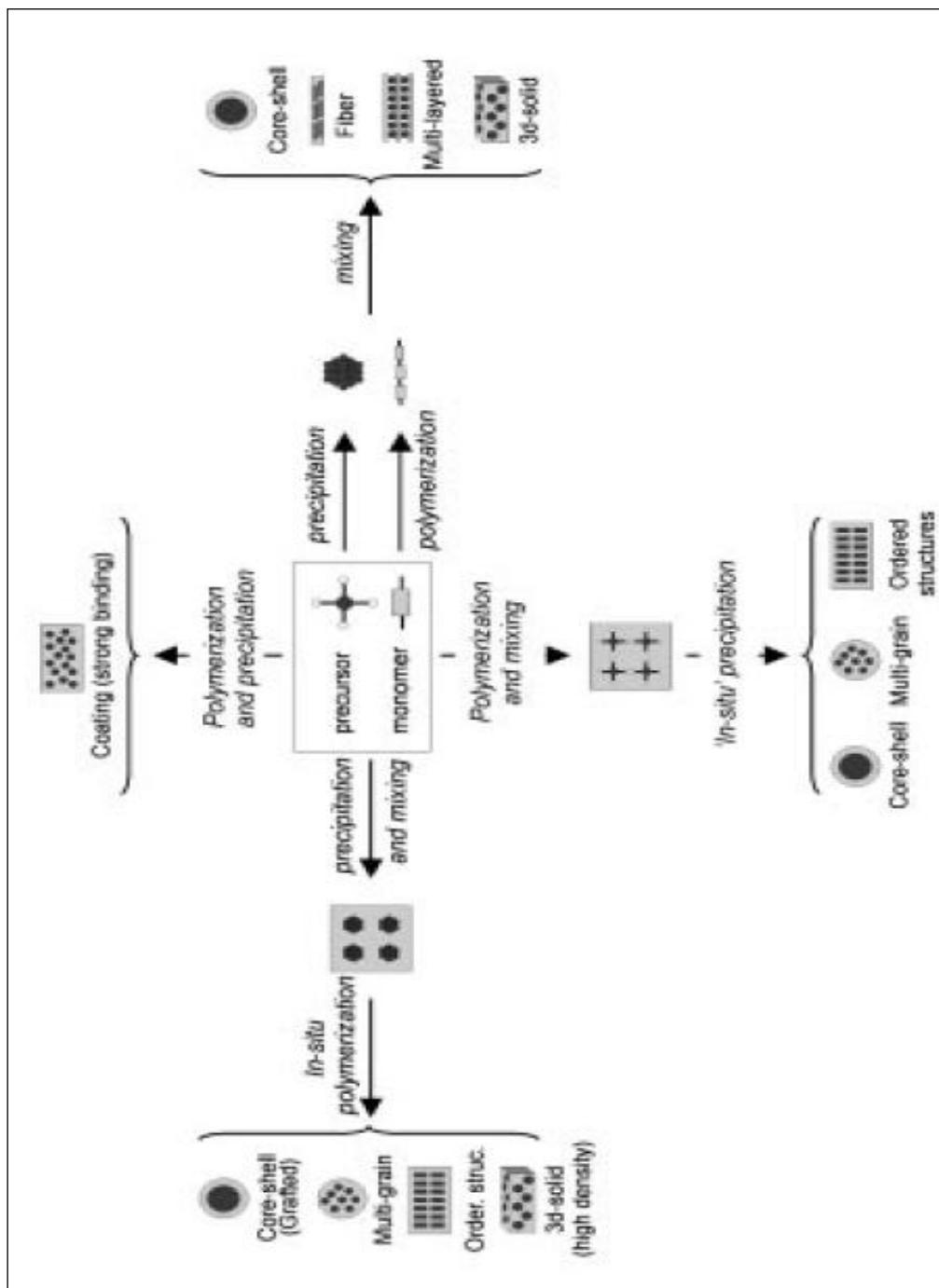
Figure 3.1. The flow chart of processing magnetic polymer nanocomposites (Mai & Yu , 2006).

3.2.1 Precipitation of the Magnetic Component

Precipitation of the magnetic components, several routes can be written as follows.

Reaction of the precursor: The choice of the precursor depends on the reaction medium such as high vacuum deposition methods use volatile organomettalic precursors or atoms, ion or molecule beams. Normal pressure vapor methods use similar volatile precursors or sprayed metal salt solutions. However, aqueous solution methods use water soluble salts, and organic solution methods use organo-mettalic soluble compounds. Typical chemical reactions to genarate the growth units are as follows:

- Redox reactions,
- Hydrolysis of metal alkoxides,
- Decomposition of metal carbonyl compounds and
- Hydrolysis of metal salts

Nucleation and growth: After the generating the growth units, following step in precipitation is the formation of nuclei which is larger than the critical size for thermodynamic stability. The production of nano particles requires that: the initial super saturation is high enough to allow fast nucleation, the size of critical nucleus is small (depends on surface tension and temperature) and the supersaturation decreases very fast nucleation in order to avoid extensive particle growth.

Aggregation: Aggregating reduces the high surface energy of the fine particles Additives that adsorb on the particle surface restrain aggregation by reducing the surface energy. In this respect, it is important to give a definition for the control of the particle size. There are some several systems that average size and the size distribution can be controlled in many ways such as controlling the gas flow, adjusting the reactions conditions, to confine the reactants in flexible nanocages, with the concentration and volume of the liquid drops, by size-sorting procedures

(magnetic separation, field-flow fractionation, size exclusion chromatography and size- selective precipitation). (Mai & Yu, 2006)

3.2.2 Mixing of Polymer and the Magnetic Component

Bulky materials and thin films can be prepared by dispersing the magnetic component in a polymer solution or a polymer melt, and then evaporating, spin-casting or cooling. The stability of the nanocomposite suspension can be reinforced by cross linking of the polymer after coating or the other procedure to produce stable suspensions employs bifunctional polymer layers. A simple way to get polymer coated particles is to precipitate the dispersion by addition of a non-solvent, and then fast cooling.

3.2.3 In situ Polymerization

The polymerization can be carried out in a dispersion of the particles in a monomer solution or in a monomer melt. Monomers are less viscous and more soluble than polymers. Hence, this route is especially suited for the preparation of nanocomposites with a high density of particles, when the polymer is insoluble or when it does not melt. In order to enhance cohesion, the polymer can be grafted to the particle surface by irradiation polymerization. Polymerization in solution is the preferred route for the fabrication of core-shell particles. This route facilities a strong particle-polymer binding by pre-activation of the particle surface with reactive residues, polymerization initiators, or the own monomer. Nanocomposite micro particles containing several magnetic nano particles in the interior have also been prepared by in-situ polymerization.

3.2.4 In situ Precipitation

In situ precipitation is rather suitable for the preparation of films and bulky materials and ensures a controlled particle growth, a regular particle-polymer interphase, a uniform distribution of particles in the matrix, and even micro structural organization. Polymer and metal precursor can be mixed by:

- Absorption of metal ions in ionic exchange resins or in polymer gels;

- Dissolution of the precursor in a polymer melt, or a polymer solution;

- Deposition of the precursor in a porous polymer by chemical, electrochemical, or vapor methods.

The modulation of the size and shape of the particles can be introduced by considering precursor/polymer ratio the molecular weight of the polymer, and the relative chain length in block copolymers.

Normally, in-situ precipitation takes full profit of the templating capacity of organic-inorganic hybrids and polymers, emulating biological processes. This method is also compatible with vapor deposition methods. In this respect, magnetic recording tapes are prepared by vapor deposition of metal vapors of a polymer substrate. (Mai & Yu, 2006)

3.3 Preparation Method of Nano-Sized Particles

In general, nano particles are used for reinforced the polymer in either physical or chemical properties in polymer nanocomposites. The transition from micro particles to nano particles provides a number of changes in physical properties. Two major factors in this area are the increase in the ratio of surface area to volume, and the size of the particle moving into the realm where quantum affects predominates. Increment in the surface areas to volume ratio which is a gradual progression as the particle gets smaller, leads to an increasing dominance of the behavior of atoms on the surface of a particle over that of those in the interior of the particle. This criteria affects both the properties of the particle in isolation and its interaction with other materials (Holister, Weener, Roman & Harper, 2003).

It is widely known that the optical, electrical and magnetic properties of materials differ with the particle sizes and with the degree of crystallinity and shape (shape anisotropy). Nowadays, different synthesis methods have been used to improve their magnetic capabilities. Studies have shown that physical properties of nanoparticles are influenced significantly by the processing techniques (Koutzarova, Kolev, Ghelev, Grigorov & Nedkov, 2008).

Because the reactants are not mixed on the atomic scale, solids with nanosize particle size cannot be prepared or treated by international methods simply. Alternative methods such as hydrothermal, sol-gel, chemical vapour deposition and microwave address this problem by achieving atomic scale mixing of reactant in gas, liquid or even solid phases (Gacitua et al., 2005).

Crystallite and particle size distribution, and inter particle spacing have the greatest impact on magnetic properties, so the ideal synthesis technique must support superior control over these parameters. Various techniques have been carried out for the synthesis of nanoparticles with definite sizes and shapes. Most of these techniques are low temperature methods, although finally firing may be required at high temperatures especially for ceramic type products. These methods enable the final product with the following characteristics such as high surface area, nanosize particles, homogenously pure improved properties and narrow particle size distribution (Koutzarova et al., 2008).

Varieties of soft chemical methods have been developed in order to reduce the particle size and obtain highly homogeneous ultra fine single-domain particles of barium hexaferrite. The glass-ceramic method, chemical co-precipitation, hydrothermal processes, the ammonium nitrate melt method, sol–gel , pyrolysis of aerosol, the mechanochemical method, auto combustion are the most popular techniques. In all these processes, precursors are used to have ultra-fine size and high surface area; hence conventional restrictions of phase equilibrium and kinetics can be easily overcome, that leads to reducing of sintering and solid-state reaction temperatures and increased sintering rate. These methods are widely known and commonly used in the synthesis of magnetic oxides. The next sections will consider some of them in detail (Koutzarova et al., 2008).

3.3.1 Vapor Condensation

Vapor condensation is generally used to make metallic and metal oxide ceramic nanoparticles and includes evoparation of a solid metal followed by rapid condensation to form nanosized clusters that settle in the form of a powder. Various approaches to vaporizing the metal can be used and variation of the medium into which the vapor is released affects the nature and size of the particles. Avoiding oxidation when creating metal nanoparticles inert gases are used, whereas a reactive oxygen atmosphere is used to produce metal oxide ceramic nanoparticles. The main advantage of this approach is to reduce contamination levels. Final particle size is controlled by variation of parameters such as gas environment, temperature and evaporation rate (Holister et al., 2003).

Chemical Vapor Synthesis (CVS) is a modified Chemical Vapor Deposition (CVD) method where the process parameters are adjusted to form nanoparticles instead of film. The entire range of reaction regimes and corresponding microstructures (epitaxial, polycrystalline, columnar, granular films and aerogel coatings as well as nanopowders) are shown in the below. Both in CVD and CVS, precursors are metal organics, carbonyls, hydrides, chlorides and other volatile compounds in gaseous, liquid or solid state. The important limitation of the CVS process is the availability of appropriate precursor materials. The energy for the conversion of the reactants into nanoparticles is supplied in hot wall (external furnace), flame (reaction enthalpy), plasma (microwave or radio frequency) and laser (photolysis or pyrolysis) reactors. Chemical Vapor Reaction (CVR), Chemical Vapor Condensation (CVC), Chemical Vapor Precipitation (CVP) are synonyms used frequently in the literature. The most important process parameters determining the quality and usability of the nanopowders are the total pressure (typical range from 100 to 100000 Pa), the precursor material (decomposition kinetics and ligands determining the impurity level), the partial pressure of the precursor (determining the production rate and particle size), the temperature or power of the energy source, the carrier gas (mass flow determining the residence time) and the reactor geometry. The nanoparticles are extracted from the aerosol by means of filters, thermophoretic collectors and electrostatic precipitators or scrubbing in a liquid. A typical laboratory

reactor that is shown schematically in the Figure 3.2 below consists of a precursor delivery system, a reaction zone, a particle collector and a pumping system. Modifications of the precursor delivery system and the reaction zone allow the synthesis of pure oxides, doped oxides, coated nanoparticles, functionalized nanoparticles and granular films. (Winterer, 2007)
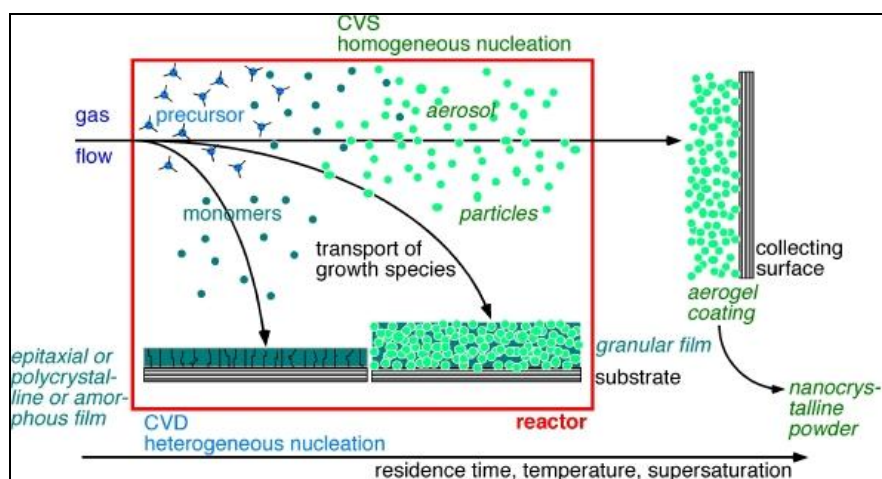
Figure 3.2 Chemical Vapour Synthesis of Nanocrystalline Powders

(Winterer, 2007)

Chemical Vapor Deposition (CVD) process may be defined as the chemical process used to produce high purity and high performance solid materials and deposition of a solid on a heated surface from a chemical reaction in the vapor phase. CVD is a common process suitable for manufacturing of fibers, powders, coatings and monolithic components. Toshiba has developed a new nanoparticle production method based on the chemical vapor deposition technique generally used to make thin films for use in large-scale integrated circuits. Both liquid and gas forms of a substance are put into a reactor. Depending on several parameters such as gas/liquid ratio, the order in which the gas and liquid are added, the temperature and the length of time during which heat is applied), different particle shapes can be created and controlled (homogenous nanoparticles can be important in many applications-nanoparticles used in a magnetic disk to record data, for example, must all be much the same size) (Gacitua et al., 2005).

Another type of evaporation method is vacuum evaporation on running liquids (VERL) method. This type of method uses a thin film of a relatively viscous materials, an oil, or a polymer, for instance on a rotating drum. A vacuum is maintained in the apparatus and the desired metal is evaporated or sputtered into the vacuum. Particles form in suspension in the liquid and can be grown to a variety of sizes (Holister et al., 2003).

3.3.2 Solid State Processes

Grinding or milling is used to create nanoparticles. Milling time, milling material and atmospheric medium affect resultant nanoparticle properties. Nanoparticles can be produced by this approach to from materials that do not readily lend themselves to the two previous techniques. Contamination from milling material can be an issue (Holister et al., 2003). The conventional solid-state method for preparing $BaFe_{12}O_{19}$ is to fire an appropriate mixture of α-Fe_2O_3 and $BaCO_3$ at very high temperatures (1150–1250°C). The resulting powder is then ground to reduce the particles' size. Although high-temperature firing provides the formation of the required ferrite phase, larger particles (>1 μm) are often obtained in this firing process. It has been shown that the theoretical intrinsic coercivities of ferrites can be approached only when the particle sizes are below 1 μm. On the other hand, grinding may present impurities into the powder and cause strains in the crystal lattices, which has unfavorable effect on the magnetic properties (Koutzarova et al., 2008).

In addition to this, ball milling has been utilized in various industries to perform size reduction for a long time. Recently, materials with novel microstructures and properties have been synthesized successfully via high-energy ball milling processes. Although different terms have been used to describe the high-energy ball milling processes, especially three terms are used to distinguish powder particle behavior during milling: mechanical alloying (MA), mechanical milling (MM), and mechanochemical synthesis (MS).

There are some inherent advantages in processing nanomaterials via high-energy ball milling techniques, such as scalability, excellent versatility and cost-

effectiveness. For this reason, high-energy ball milling techniques are well suited for manufacturing large quantity of nanomaterials (Gacitua et al., 2005). To get rid of these problems, various soft chemical methods have been developed in order to reduce the particle size and obtain highly homogeneous ultra fine single-domain particles of barium hexaferrite (Koutzarova et al., 2008).

3.3.3 Chemical Methods

3.3.3.1 Polymerized Complex Method

Wet chemical method using polymeric precursor based on the Pechini process has been employed to prepare a wide variety of ceramics oxides. The process introduces several advantages for processing ceramic powders such as direct and precise control of stoichiometry, uniform mixing of multicomponents on a molecular scale, and homogenity (Gacitua et al., 2005).

The citric acid precursor method originated from the Pechini method. Pechini developed this method in 1967 and applied for patent in the United States (Patent No. 3 330 697). In the precursor method, the metallic salts are dissolved in water to have the required metallic ions well mixed. The metallic ions are then chelated by a poly-acid (e.g., citric acid), and esterification of chelated cations is carried out by adding poly-alcohol (e.g., ethylene glycol) at appropriate temperatures. After the dehydration, a solid ester precursor with well-mixed metallic ions can be obtained. The solid precursor is subjected to proper heat treatment to form the final ceramic particles. Lucchini reported that using pectic acid to chelate barium and iron ions in an aqueous solution of nitrates and heating in air at 700 $^{\circ}$C can produce crystalline barium ferrite with particle sizes less than 1 μm in diameter (Koutzarova et al., 2008).

3.3.3.2 Hydrothermal Synthesis

The hydrothermal process is used to synthesize ultra-fine, pure, stress free barium hexa ferrite powder with a narrow size distribution at relatively low temperature

(200–300°C). This synthesis uses different precursors such as $Ba(NO_3)_2$ and $Fe(NO_3)_3 \cdot 9H_2O$ mixtures in the presence of $NaOH/KOH/NH_4OH$, $(C_2H_5)_4NOH$; $FeOOH$ and $Ba(OH)_2$ mixture; $\alpha\text{-}Fe_2O_3$ and $Ba(OH)_2$ mixtures; $FeCl_3$ and $Ba(OH)_2$ mixtures. Hydrothermal reactions are usually performed in closed vessels. The reactants are either dissolved or suspended in a known amount of water and are transferred to acid digestion reactors or autoclaves. Under hydrothermal conditions, reactants otherwise difficult to dissolve can go into solution and reprecipitate (Koutzarova et al., 2008).

The term 'hydrothermal' came from the earth sciences, where it implied a regime of water pressures and high temperatures. For typical H–T research, one needs a high temperature, high-pressure apparatus called 'autoclaves' or 'bombs'. Hydrothermal synthesis includes H_2O both as a catalyst and occasionally as a component of solid phases in the synthesis at elevated temperature (> 100°C) and pressure (> a few atmosphere). At present, one can get many autoclaves to cover different p–t ranges and volumes. For hydrothermal experiments the requirements for starting materials are; as pure as possible, accurately known composition, as homogeneous as possible and as fine as possible, etc. (Somiya & Roy, 2000)

3.3.3.3 The Low Temperature Combustion

This route is based on the gelling and subsequent combustion of an aqueous solution containing salts of the desired metals and some organic fuel, giving a voluminous and fluffy product with large surface are. This kind of method has been proved to be a time-saving, new, extremely facile and energy-efficient route for synthesis of ultra-fine powders. By using this method, Huang reported that synthesized barium hexaferrite powders based on the combustion of nitrate-citrate gels due to an exothermic redox reaction between nitrate and citrate ions. The particles have sizes between 80 and 120 nm and $M_s = 59.36$ emu.g^{-1} and $H_c = 4.4 \times 10^5$ Am^{-1} (Koutzarova et al., 2008). Figure 3.3 shows systematic of the low temperature combustion.
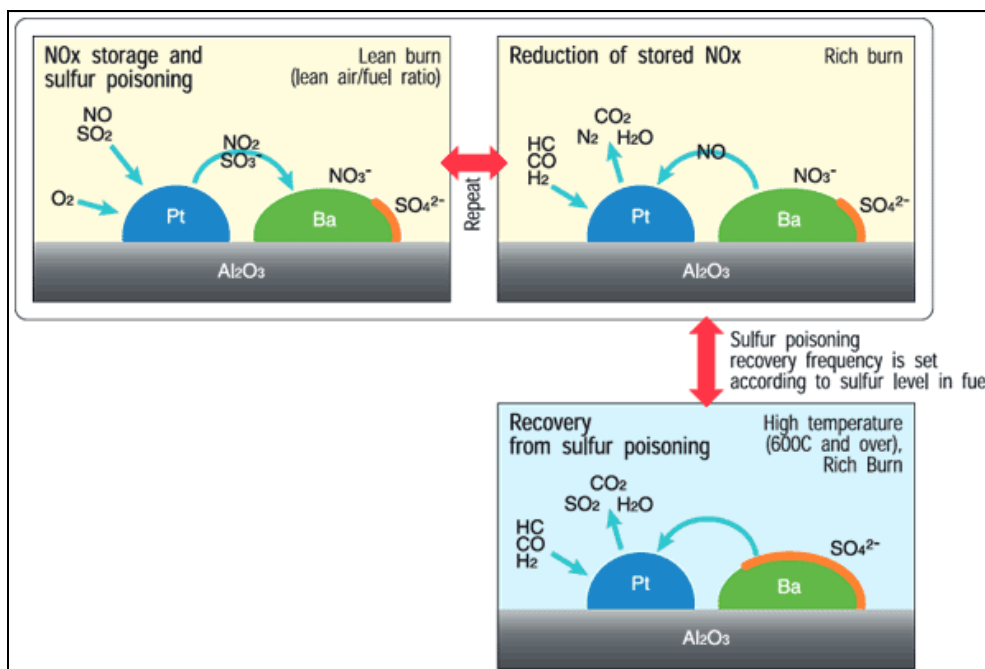
Figure 3.3 Systematic of the low temperature combustion (Japan Petroleum Energy Center, 2006)

3.3.3.4 Aerosol Process

It is a solution of the cations which passed through an aerosol generator in the form of fine droplets, which are subsequently dried to form fine powders on passage through vacuum. The particles are then carried through a heated reactor tube in which the precursor compounds react to yield fine particulates, which are then collected on a filter. Monosized spherical particles can also be obtained by controlling the droplet size and contamination can be avoided to a large extent by this method; powders having various size distributions can also be synthesized (Koutzarova et al., 2008).

The chemical co-precipitation method is a cheap and easy choice for mass production. In this process, the cations are generally precipitated from solutions, such as hydroxides or carbonates. Co-precipitation of multivalent cations in a multicomponent system is difficult because the precipitating agent such as OH^- and CO_3^{2-} form insoluble species with cations which have approximately the same solubility product only under very narrow boundary condition of pH, temperature, dielectric constant of solvent. In the hydroxide process, the cations are precipitated

from the solutions by using NaOH/KOH or NH_4OH as precipitating agent. The carbonates are precipitated from the metal salts solution by adding Na/K-carbonate or $(NH_4)_2CO_3$. The co-precipitation method was used to prepare barium ferrite and showed that by heating the co precipitates at relatively low temperatures ($\leq 800 \circ C$), submicron $BaFe_{12}O_{19}$ particles can be obtained. The influence of the heat treatment temperature on barium hexaferrite's magnetic properties was studied in detail. In general, this method does not allow one to control the size and size distribution of the particles. In order to overcome these difficulties, the micro emulsion method was proposed, which will be discussed in more detail later (Koutzarova et al., 2008).

3.3.3.5 Sol-Gel Method (Wet Chemical Synthesis of nanomaterials)

In the sol–gel synthesis the term sol refers to a suspension or dispersion of discrete colloidal particles, while gel represents a colloidal or polymeric solid containing a fluid component, which has an internal network structure wherein both the solid and fluid components are highly dispersed. The cations first form a sol of either hydroxides or citrates or acetates. The discrete colloidal particles slowly coalesce together to form a rigid gel. Since the particle sizes are very fine, these gels can be calcined at much lower temperatures than the conventionally derived powders to obtain a homogeneous product. Atomic level mixing of constituents in the sol–gel process leads to the formation of single-phase products much more easily than by other process. The purity, microstructure and properties of the product can be controlled by the proper selection of starting precursors, solvent, pH of sol, calcinations temperature and processing environment. The main problems in the hexaferrite preparation by the sol–gel technique are the gel formation and the deviation of measured and expected values of the specific saturation magnetization.

To sum up the sol-gel process, as the name implies, involves the evolution of inorganic networks through the formation of a colloidal suspension (**sol**) and gelation of the sol to form a network in a continuous liquid phase (**gel**). The precursors for synthesizing these colloids consist usually of a metal or metalloid element surrounded by various reactive ligands. The starting material is processed to form a

dispersible oxide and forms a sol in contact with water or dilute acid. Removal of the liquid from the sol yields the gel, and the sol/gel transition controls the particle size and shape. Calcination of the gel produces the oxide.

Sol-gel processing refers to the hydrolysis and condensation of alkoxide-based precursors such as Si (OEt) $_4$ (tetraethyl orthosilicate, or TEOS). The reactions involved in the sol-gel chemistry based on the hydrolysis and condensation of metal alkoxides M(OR) can be described as follows:

$$MOR + H_2O \rightarrow MOH + ROH \text{ (hydrolysis)} \tag{3.1}$$

$$MOH + ROM \rightarrow M\text{-}O\text{-}M + ROH \text{ (condensation)} \tag{3.2}$$
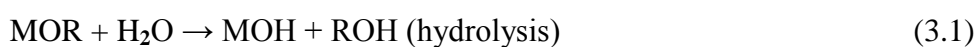
Sol-gel method of synthesizing nanomaterials is very popular amongst chemists and is widely employed to prepare oxide materials.

The sol-gel process can be characterized by a series of distinct steps.

Step 1: Formation of different stable solutions of the alkoxide or solvated metal precursor (the sol).

Step 2: Gelation resulting from the formation of an oxide- or alcohol- bridged network (the gel) by a polycondensation or polyesterification reaction that results in a dramatic increase in the viscocity of the solution.

Step 3: Aging of the gel (Syneresis), during which the polycondensation reactions continue until the gel transforms into a solid mass, accompanied by contraction of the gel network and expulsion of solvent from gel pores. Ostwald ripening (also referred to as coarsening, is the phenomenon by which smaller particles are consumed by larger particles during the growth process) and phase transformations may occur concurrently with syneresis. The aging process of gels can exceed 7 days and is critical to the prevention of cracks in gels that have been cast.

Step 4: Drying of the gel, when water and other volatile liquids are removed from the gel network. This process is complicated due to fundamental changes in the structure of the gel. The drying process has itself been broken into four distinct steps: (i) the constant rate period, (ii) the critical point, (iii) the falling rate period, (iv)the second falling rate period.

If isolated by thermal evaporation, the resulting monolith is termed a *xerogel*. If the solvent (such as water) is extracted under supercritical or near super critical conditions, the product is an *aerogel*.

Step 5: Dehydration, during which surface- bound M-OH groups are removed, there by stabilizing the gel against rehydration. This is normally achieved by calcining the monolith at temperatures up to $800^{o}C$.

Step 6: Densification and decomposition of the gels at high temperatures (T>$800^{o}C$). The pores of the gel network are collapsed, and remaining organic species are volatilized. The typical steps that are involved in sol-gel processing are shown in the schematic diagram below.
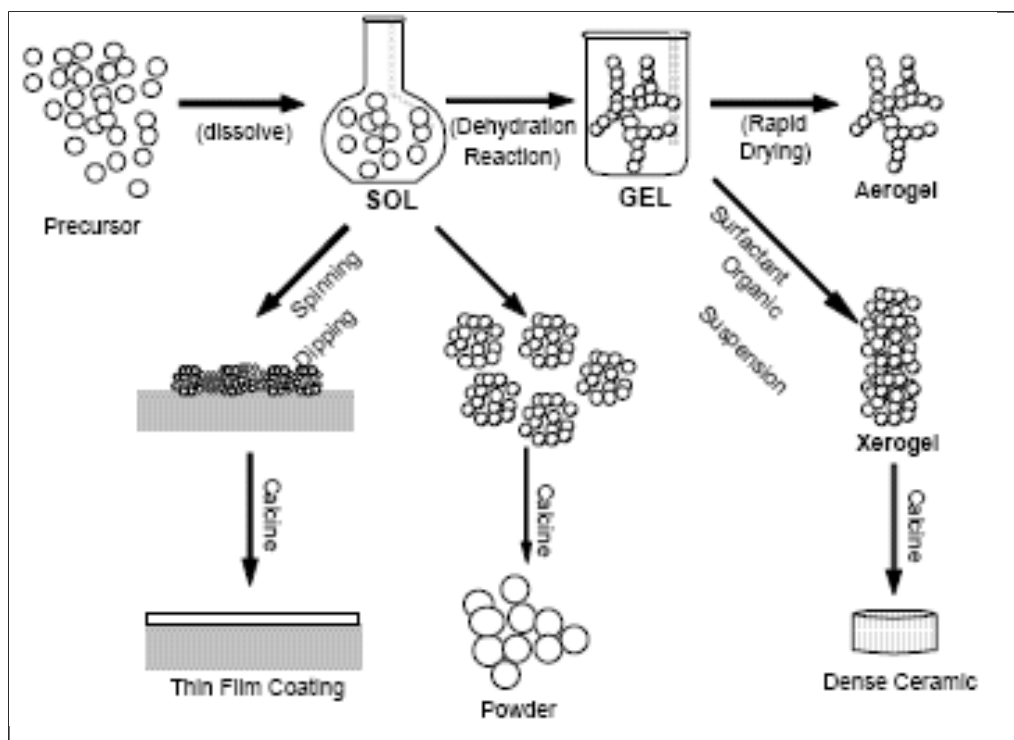
Figure 3.4 Route of the sol-gel (Gitam University, 2009)

The interest in this synthesis method arises due to the possibility of synthesizing nonmetallic inorganic materials like glasses, glass ceramics or ceramic materials at very low temperatures compared to the high temperature process required by melting glass or firing ceramics.

The most important technical difficulties to overcome in developing a successful bottom-up approach is controlling the growth of the particles and then stopping the newly formed particles from agglomerating. Other technical issues are ensuring the reactions are complete so that no unwanted reactant is left on the product and completely removing any growth aids that may have been used in the process. In addition to this, production rates of nano powders are very very low by this process. The main advantage is one can get monosized nano particles by any bottom up approach (Gitam University, 2009).

CHAPTER FOUR
EXPERIMENTAL METHOD

In this study our aim was to investigate the thermal, microstructural, phase, mechanical and magnetic properties of barium hexaferrite powders and polymer nanocomposites that reinforced with undoped and Mn-Cu-Ni doped barium hexaferrite powders.

4.1 Materials

In order to obtain polymer nanocomposites, nanoparticles including barrium hexaferrite were synthesized in the present study. Barrium hexaferrite powders were synthesized from highly pure precursor materials. Barium nitrate ($Ba(NO_3)_2$, 99.999%, Aldrich), ferric citrate mono hydrate ($C_6H_5FeO_7.H_2O$, 18-20%, Fluka), Cobalt (II) nitrate hexahydrate ($Co(NO_3)_2.6H_2O$, %99,999), manganese (II) nitrate tetrahydrate ($Mn(NO_3)_2.4H_2O$, 98.5%, Merck), copper (II) nitrate trihydrate ($Cu(NO_3)_2.3H_2O$, 99-104%, Fluka), strontium nitrate ($Sr(NO_3)_2$) and nickel (II) nitrate hexahydrate ($Ni(NO_3)_2.6H_2O$, 99.999%, Aldrich) as precursors, citric acid monohydrate ($C_6H_8O_7.H_2O$, 99.5-100.5%, Riedel-de Haen) as a chelating agent, ammonium hydroxide (26%, NH_4OH, Riedel-de Haen) as pH regulator were used to produce barium ferrite hexaferrite powders.

Polymeric materials which is called as PVC- 39 were provided from PETKIM Inc., Izmir, Turkey. PVC is the most widely used thermoplastic polymer after polyethylene and polypropylene. In term of revenue generated, it is the most valuable product of the chemical endustry. Table 4.1 shows properties of PVC S-39.

Table 4.1 Properties of PVC S-39 (PETKİM A.Ş.)

Properties	Value
Density	1390 kg/m^3
Young's modulus (E)	2900-3300 MPa
Tensile strength(σ_t)	50-80 MPa
Elongation at break	20-40%
Notch test	2-5 kJ/m²
Glass temperature	82 °C[1]
Melting point	100–260 °C
Vicat B	85 °C
Heat transfer coefficient (λ)	0.16 W/(m·K)
Effective heat of combustion	17.95 MJ/kg
Linear expansion coefficient (α)	8 10^{-5}/K
Specific heat (c)	0.9 kJ/(kg·K)
Water absorption (ASTM)	0.04-0.4
Price	0.5-1.25 €/kg

4.2 Processing of Nanocomposite Materials

4.2.1 Preparation of Barium Hexaferrite Powders

Barium ferrite powders with atomic scale were prepared using citrate sol-gel process. With this respect, $BaFe_{12}O_{19}$, $BaFe_{12-x}(Mn_{0.5}Co_{0.5}Sr)_{x/2}O_{19}$), $BaFe_{12-x}(Mn_{0.5}Co_{0.5}Ni)_{x/2}O_{19}$,$BaFe_{12-x}(Mn_{0.5}Cu_{0.5}Ni)_{x/2}O_{19}$ and $BaFe_{12-x}(Mn_{0.5}Cu_{0.5}Sr)_{x/2}O_{19}$ for x=2 were synthesized as reinforced nanoparticles. Stoichiometric amounts of barium nitrate $Ba(NO_3)_2$, ferric citrate $C_6H_5FeO_7.H_2O$, manganese nitrate tetrahydrate $Mn(NO_3)_2.4H_2O$, copper nitrate trihydrate $Cu(NO_3)_2.3H_2O$, citric acid $C_6H_8O_7.H_2O$ were used to produce main phases including $BaFe_{12-x}(Mn_{0.5}Cu_{0.5}X)_{x/2}O_{19}$ and $BaFe_{12-x}(Mn_{0.5}Co_{0.5}X)_{x/2}O_{19}$.

Barium nitrate and ferric citrate were dissolved in citric acid solution. The ratios of citric acid: metal = 3 and Fe: Ba=11 were used from the studies that were performed by Dong and Zhan, 2006. After that, both solutions were mixed in this experiment. Manganese nitrate, copper nitrate, strontium nitrate and zirconium isopropoxide as

precursors (if required) and doping agent were subsequently added to the solution in the stoichiometric ratios. These solutions were vigorously mixed by magnetic stirrer until the transparent solution was obtained. Ammonium hydroxide was added until reaching of the pH value of the solution to 7 at room temperature and then mixed by magnetic stirrer. Thus it was aimed to provide homogenous suspension and stable pH condition in the solution after whole solution preparation. The solution was kept in water bath at $80^{o}C$ for 15 hours. Therefore, the water in the solution was gradually removed and wet gel with high viscosity was obtained. The wet gel was treated at 180 ^{o}C for 15 hours in Nüve KD400 oven (Nüve, Inc., Ankara, Turkey) to prepare dry gel. The dry gel was exposed to pre-sintering process at $550^{o}C$ for 6 hours to evaporate impurities and then was sintered at $1000^{o}C$ for 5 hours in ash oven in air (Ghasemi, Liu & Morisako, 2007, Ghasemi, Saatchi, Salehi, Hossienpour & Liu, 2006). The flow chart of sol-gel citrate process to produce barium ferrite powders was shown in Figure 4.1.

4.2.2 Preparation of Polymer Nanocomposites

Polymeric nanocomposites were produced by reinforcing undopped barium hexaferrite and Mn-Cu-Ni dopped barium hexaferrite powders at 140 ^{o}C for 10 minutes in air and at 50 rpm of speed using Brabender Plasticorder PL 2000 W 30 "mixer head". After this procedure, the composites were processed to shape at 160 ^{o}C, for 10 minutes and at 5 MPa of loading in hot press machine.

4.3 Characterization

4.3.1 Differential Thermal Analysis - Thermogravimetry (DTA-TG)

The thermal behaviors of the barium ferrite powders, which were dried at 180 ^{o}C for 6 hours in air, were evaluated to determine the decomposition and phase formation at a heating rate of $10^{o}C/min$ in the temperature range of 0–1200 ^{o}C under an oxygen atmosphere with a DTA–TG machine (DTG-60H, Shimadzu, Kyoto, Japan). The changes in temperature with exothermic and endothermic reactions were

```
┌─────────────────────────────────────────┐
│  Ferrite citrate and barium nitrate are  │
│  dissolved separately with citric acid   │
│  in distilled water (Molar ratio of      │
│  CA: Metal=3, Fe: Ba=11)                 │
└─────────────────────────────────────────┘
                     │
                     ▼
┌─────────────────────────────────────────┐
│  Mixing the solutions with magnetic      │
│  stirrer until obtained transparent      │
│  solutions                               │
└─────────────────────────────────────────┘
                     │
                     ▼
┌─────────────────────────────────────────┐
│  Adding  manganese nitrate, copper       │
│  nitrate, cobalt nitrate, nickel nitrate │
│  and stronsium nitrate (optional)        │
└─────────────────────────────────────────┘
                     │
                     ▼
┌─────────────────────────────────────────┐
│  Dropping the amonium hydroxide          │
│  solution until obtain the pH 7          │
└─────────────────────────────────────────┘
                     │
                     ▼
┌─────────────────────────────────────────┐
│  Heat treatment at 80 ˚C for 15 hours    │
│  in water bath until whole water         │
│  evoporates                              │
└─────────────────────────────────────────┘
                     │
                     ▼
┌─────────────────────────────────────────┐
│  Heat treatment at 180 ˚C for 15 hours   │
│  in oven until having particles like ash │
└─────────────────────────────────────────┘
                     │
                     ▼
┌─────────────────────────────────────────┐
│  Pre-sintering at 550 ˚C for 6 hours     │
└─────────────────────────────────────────┘
                     │
                     ▼
┌─────────────────────────────────────────┐
│  Sintering at 1000 ˚C for 5 hours        │
└─────────────────────────────────────────┘
                     │
                     ▼
┌─────────────────────────────────────────┐
│  Undoped and doped barium hexaferrite    │
│  powders                                 │
└─────────────────────────────────────────┘
```
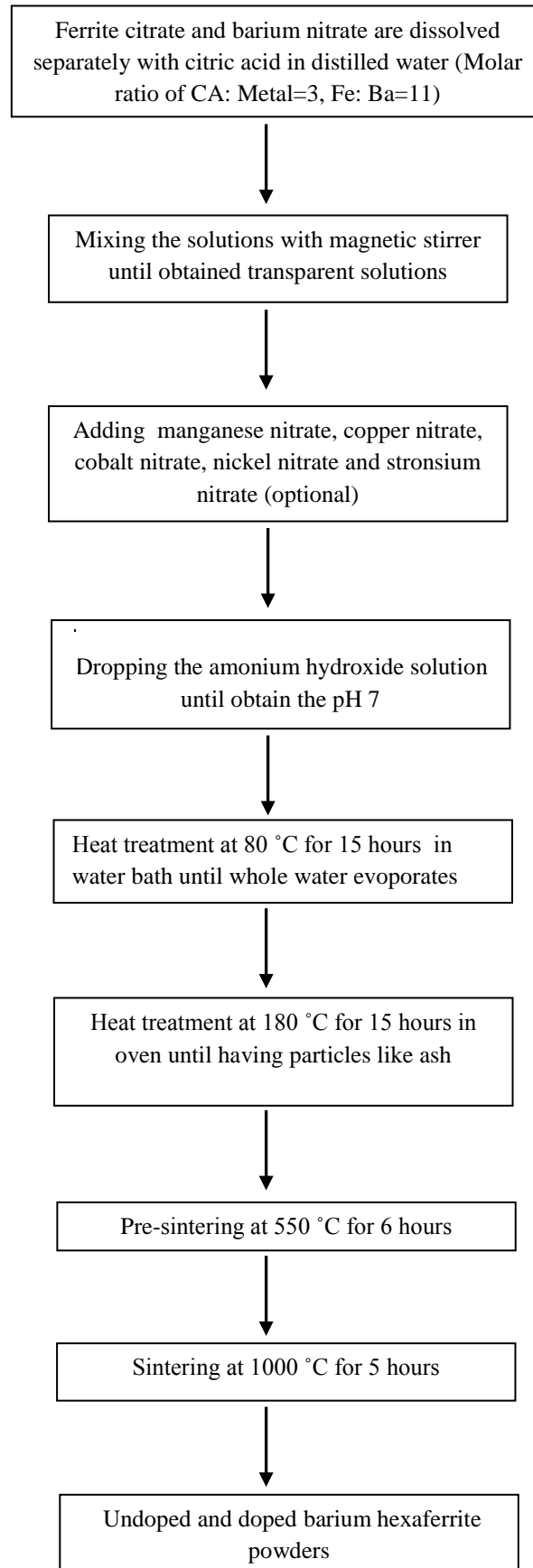
Figure 4.1 The flow chart of sol-gel citrate process

measured using differential thermal analyzer (DTA) and the mass variations in materials such as water loss, remove of organic materials were measured using thermogravimetry (TG). This equipment has a heating range between 1-50 C/ sec. up to 1500 C.

4.3.2 X-Ray Diffaraction (XRD)

Phase analysis of the barium ferrite powders and polymer nanocomposites were carried out by means of a Rigaku D Max-2200/PC X-ray diffractometer (Rigaku Corp., Tokyo, Japan) at with a CuK$_\alpha$ irradiation (wavelength, λ=0.15418 nm) by both θ-2θ mode and 2θ scan mode. The diffracted X-ray beam was collected by scanning the detector between $2\theta = 3°$and $90°$. Grain size determination of powders were performed with X-Pert using the Scherer Formula (Eq. 4.1).

Scherer Equation: $L_c = 57.3 \lambda [FWHM (\cos \theta)]^{-1}$ Formula. (4.1)

This programme computes the crystalline size with full width half maximum (FWHM). To compute the crystalline size, the biggest peak of the obtained phase is chosen and computes the FWHM shown in Figure 4.2.
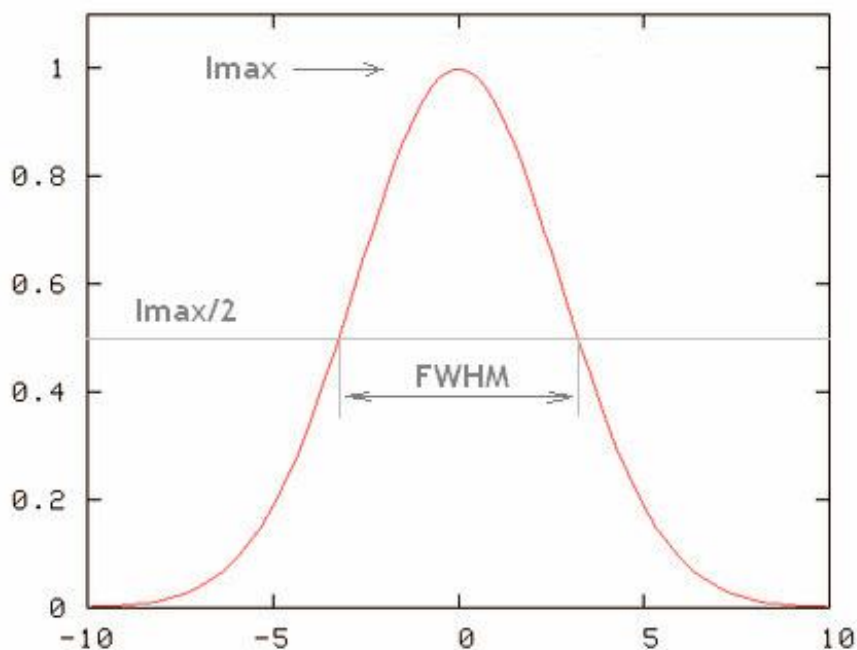

Figure 4.2. Full width at half maximum (FWHM) intensity (Vahaplar, 2007)

The diffractometer used for the measurements X-ray diffractometer using a Cu K_α X-ray source. The wavelength of the Xray is $\lambda_{K\alpha l}$= 0.15406 nm. The sample is exposed to the X-rays at an angle θ and reflected rays are detected at an angle 2θ with respect to the original beam (Vahaplar, 2007).

4.3.3 Scanning Electron Microscope (SEM)

The surface morphology of the barium ferrite powders and polymer nanocomposites were examined through a JEOL JJM 6060 scanning electron microscope attached to an energy-dispersive spectroscopy apparatus) (JEOL Ltd., Tokyo, Japan).

Scanning electron microscope is one of the most important instrument for investigating the microstructure of metallic materials. Primary use of the scanning electron microscope is to produce high-resolution and depth-of-field images of sample surfaces. A second use is to provide chemical analyses of micron-sized areas of the structure revealed on these surfaces. Additional to image formation and microchemical analysis, the scanning electron microscope provides some other functions. These are; (1) the use of channeling patterns to evaluate the crystallographic orientation of micron-sized region, (2) the use of backscattered detectors to reveal grain boundaries on unetched samples and domain boundaries in ferromagnetic alloys, (3) the use of voltage contrast, electron beam induced current and cathodoluminescence for such purposes as characterization and failure analysis of semiconductor devices (Dokumaci, 2007).

4.3.4 Dynamic Ultra Hardness (DUH)

Mechanical properties of nanocomposite materials were determined using dynamic ultra hardness (DUH, Shimadzu DUH- W201, DUH-W201S) which contains six loading method including Indentation, Load-, Unload, Cycle, Preset Indentation Depth, Step Load Test, Step Load-Unload.

Indentation hardness has been the most commonly used technique to measure the mechanical properties of materials. It has been considered as a principal parameter for mechanical characterization of materials. The physical background of load-indentation depth behaviour of single crystals on a nanometer scale has been a matter of intensive experimental and theoretical studies.
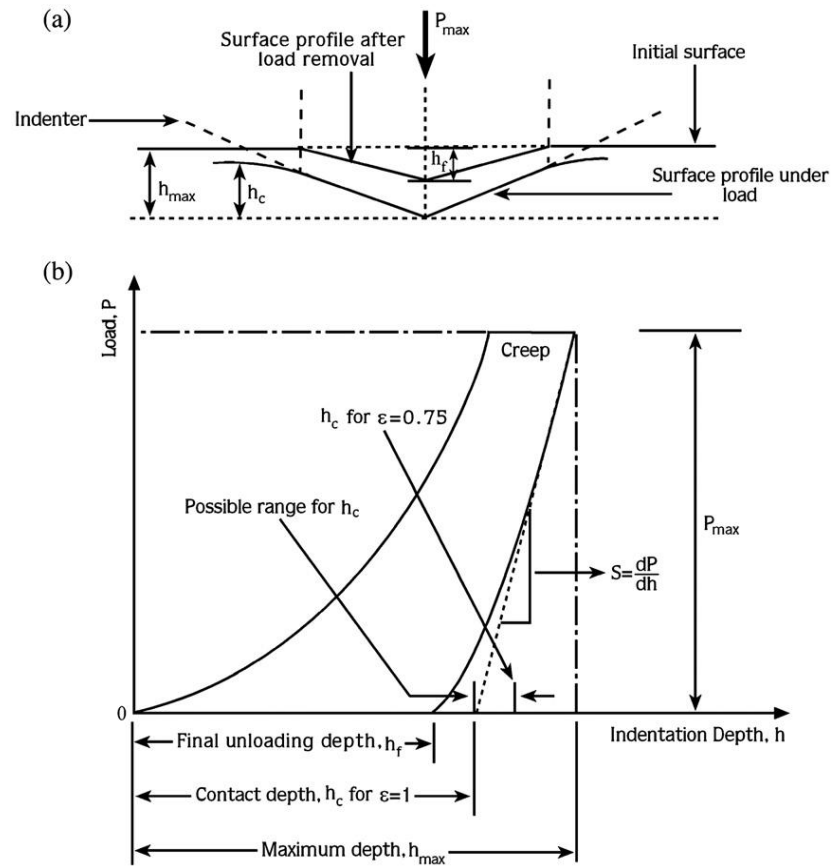

Figure 4.3. Schematic plots of a) cross-section of an indentation and b) a typical load-indentation depth curve generated during a depth-sensing   nanoindentation experiment, indicating key parameters needed for analysis. (Sahin, Uzun, Kölemen, & Ucar, 2008)

The method for determining the mechanical properties of solids is the depth-sensing nanoindentation (DSI) or dynamic indentation method. This method offers great advantages over the conventional indentation test in two aspects. First, apart from hardness (or strength), the method can provide well-defined mechanical parameters such as elastic modulus of the interfacial zone. Second, the load and

depth of an indentation are continuously monitored (Figure 4.3) and optical observation and measurements of the diagonal lengths of the indent/impression, which can be difficult and subjected to inaccuracy, are no longer required (Sahin, Uzun, Kölemen, & Ucar, 2008).

4.3.5 Vibrating Sample Magnetometer (VSM)

The magnetic properties of the barium ferrite powders and polymer nanocomposites were measured at room temperature on a vibrating sample magnetometer (VSM, Lakeshore 736, 7400 Series) in a maximum applied field of 20000 Gauss. From the obtained hysteresis loops, the saturation magnetization (M_s) and coercivity (H_c) were determined.

# CHAPTER FIVE
RESULTS AND DISCUSSION

5.1 DTA-TG Analysis

Thermal behavior of Ba and Fe based xerogel powder samples, which were dried at 180 ^{o}C for 6 hours in air, was evaluated at a heating rate of 10 °C/min under oxygen atmosphere by DTA/TG analysis in order to determine the temperature of decomposition and phase formation, and to obtain an optimum heat treatment regime. Figure 5.1 demonstrate DTA-TG curves of powder samples based on $BaFe_{12}O_{19}$ and $BaFe_{12-x}(Mn_{0.5}Cu_{0.5}Ni)_{x/2}O_{19})$ for x=2, respectively. The peaks between 100 and 150 ^{o}C was due to removal of solvent in the nature and the peaks between 200 and 300 ^{o}C were the results of degradation of the carbon based organic matters due to precursors materials, chelating agents and solvents. In addition, the decomposition of the precursors consisting of NO_3 was carried out at 300-400 ^{o}C as seen the figures. We have a good agreement with literature (Carp, Barjega, Segal & Brezeanu, 1998). Moreover TG analysis together with DTA analysis was carried out to give the results of weight loss of the powder samples at the same temperature range. As the figures, the weight loss of ($BaFe_{12}O_{19}$), $BaFe_{12-x}(Mn_{0.5}Cu_{0.5}Ni)_{x/2}O_{19})$) powders were respectively 74.6% and 66.61 % for temperatures ranging from 0 to 1200 ^{o}C. In this range of the thermal treatment, the weight loss was due to solvent removal and combustion of carbon-based materials. There was slowly weight loss due to remove solvents as to 200 ^{o}C. The weight was sharply lost due to remove organic materials as to 270 ^{o}C. The weight loss can be due to evaporation of Mn or Cu from 600 to 800 ^{o}C.

The exothermic and endothermic reactions occur in a temperature range of about 100 and 1200 ^{o}C. There are four different steps including removal of solvent based materials, combustion of carbon based content, and formation of oxides and barium hexa ferrite formation. The procedure of heat treatment to produce barium ferrite powder was determined as DTA-TG results. As a result of that, the xerogel was treated at 80 ^{o}C for 15 h to remove water in the form, and then treated to produce dry

gel at 180 °C for 15 h in an oven. Subsequently the powders were sintered process at 550 °C for 6 h and and at 1000 °C for 5 h for transforming oxide form and then completely ferrite form.
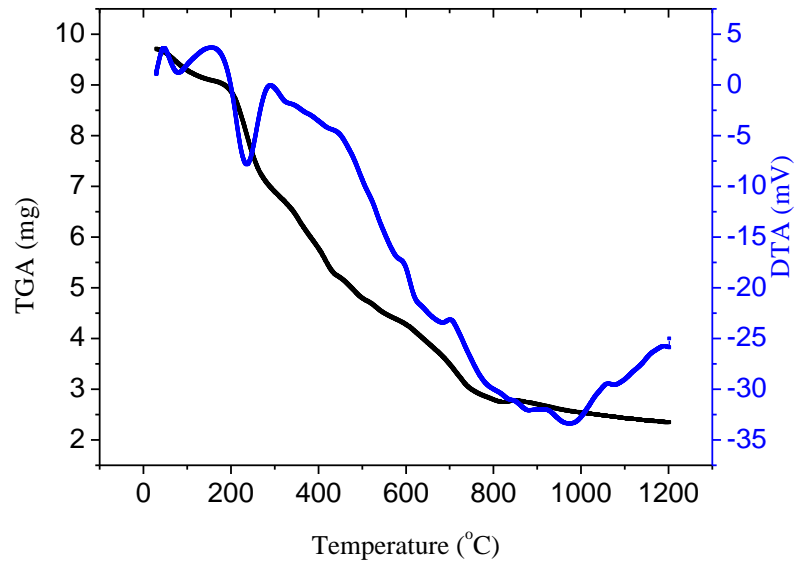
(a)
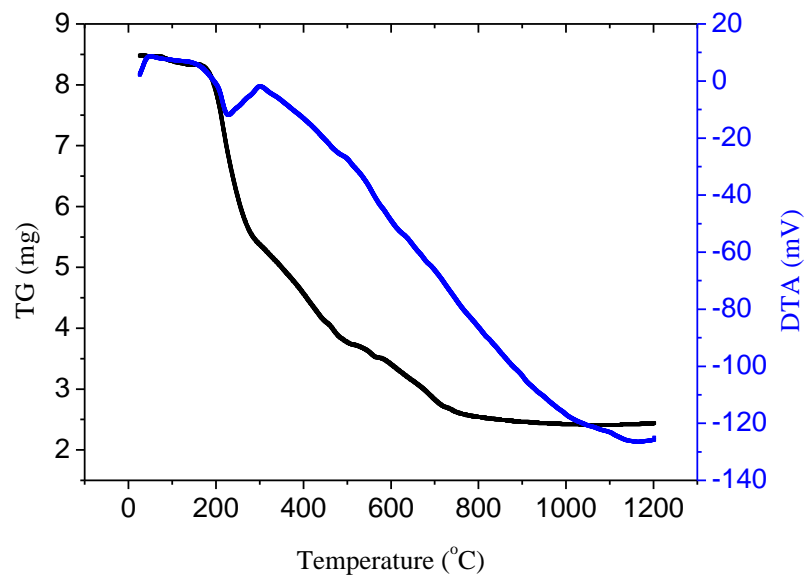
(b)

Figure 5.1 DTA-TG result of (a) undoped barium hexaferrite and
(b) Mn-Cu-Ni doped barium hexaferrite powders

5.2 Phase Analysis

Figure 5.2 depicts XRD patterns of barium hexaferrite based powders. Figure 5.2.a presents XRD pattern of the purchased nano powder from Aldrich and Figures 5.2 b, 5.2 c, 5.2 d, 5.2 e and 5.2f show XRD patterns of $BaFe_{12}O_{19}$, $BaFe_{12-x}(Mn_{0.5}Co_{0.5}Sr)_{x/2}O_{19}$, $BaFe_{12-x}(Mn_{0.5}Co_{0.5}Ni)_{x/2}O_{19}$, $BaFe_{12x}(Mn_{0.5}Cu_{0.5}Ni)_{x/2}O_{19}$, and $BaFe_{12-x}(Mn_{0.5}Cu_{0.5}Sr)_{x/2}O_{19}$, powders produced using sol-gel citrate process. In XRD pattern of the nanopowder purchased from Aldrich, JCPDS (027-1029) barium ferrite powders were clearly identified.

The undoped hexaferrite powders phase identification is shown in Figure 5.2 b. The purity of barium hexaferrite was mainly obtained except a few peaks of hematite as seen in the figure. The presence of barium ferrite phase and also a little amount of iron oxide (Fe_2O_3) phase in the pattern observed in the powders in Figure 5.2 b. It is indicated from the literature, patterns at the same angles with different intensities represents that the doping elements replaced with Fe, thus the required phases was obtained.

Figure 5.2 e shows the Mn-Cu-Ni doped barium hexaferrite powder. $CuMn_2O_4$ phase was indentified with its major peak. XRD pattern of Mn-Cu-Sr doped barium hexaferrite is illustrated in Figure 5.2.f. As seen above the required phases was obtained, that the molecular structure seems to like $BaFe_{12-x}(Mn_{0.5}Cu_{0.5}Sr)_{x/2}O_{19}$. The identified phase of Mn-Co-Ni doped powder is presented in Figure 5.2.d. Barium hexaferrite and $NiFe_2O_4$ phases were obtained. In Figure 5.2.c Mn-Co-Sr doped barium hexa ferrite was examined. Barium hexaferrite and $Ba_{0.5}Sr_{0.5}Fe_{12}O_{19}$ phases was obtained.

Concerning with phase structure of nanocomposites, XRD patterns of raw PVC S-39 polymer, nanocomposites that reinforced with and without undoped barium hexaferrite powders were shown in Figure 5.3. Generally speaking, raw PVC polymeric material displays an amorphous structure (see Figure 5.3.a for details). XRD pattern of the polymeric nanocomposite reinforced with the undoped barium hexaferrite powder was given in Figure 5.3.b. The amorphous structure of the PVC

was detected in the range of 3 and 30° angles. It is clear to see in Figure 5.3.b that the phase of crystalline structure of barium hexaferrite is shown after 30°. Figure 5.3.c represents the XRD pattern of the polymeric nanocomposite reinforced with Mn-Cu-Ni barium hexaferrite. As similar previous phases, the same structures can be seen from this figure. It can also seen from Figure 5.3.c that the amorphous structure of PVC was detected between 3° and 30° angles. In addition, crystalline phases of barium hexaferrite and $CuMn_2O_4$ are presented.
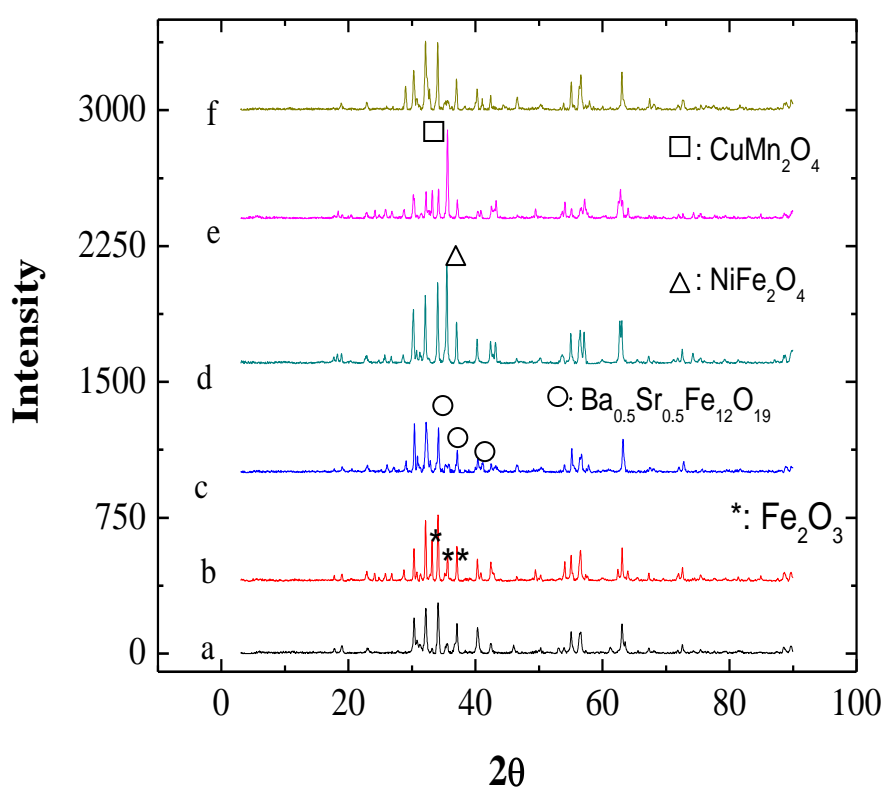
Figure 5.2 XRD patterns of (a) commercial nano powder, (b) undoped barium hexaferrite, (c) Mn-Co-Sr (d) Mn-Co-Ni (e) Mn-Cu-Ni, and (f) Mn-Cu-Sr, doped   barium hexaferrite

In Figure 5.2, XRD pattern of undoped barium ferrite still contains a little amount of hematite. It is reported that the preheating at 400-500 ^{o}C of gel prepared by sol-gel process prevented formation of α- Fe_2O_3 phases in the barium ferrite structure (Zhong et al., 1997). In this study, the presence of Fe_2O_3 phase was still observed in the structure in spite of their preheating processing at 550 ^{o}C for 6 h. Mn-Cu-Ni, Mn-Co-Ni and Mn-Co-Sr doped barium hexaferrite powders have different phases such

as $CuMn_2O_4$, $NiFe_2O_4$, $Ba_{0.5}Sr_{0.5}Fe_{12}O_{19}$. It was determined that the iron element substituted with Mn and Ni elements and these elements were embedded in barium ferrite structure. There were also some different phases in the structure. The sol-gel method is very proper process for preparing multicomponent oxides at relatively low temperatures. The sol-gel process provides not only reducing the temperature of heat treatment but also controlling of homogeneity and microstructure. In this study, the XRD patterns obtained were generally complicated and have given various phases in the structures as agreement with the literature. (Pramanik, Fujii, Nakanishi, Takada & Seok, 2006).
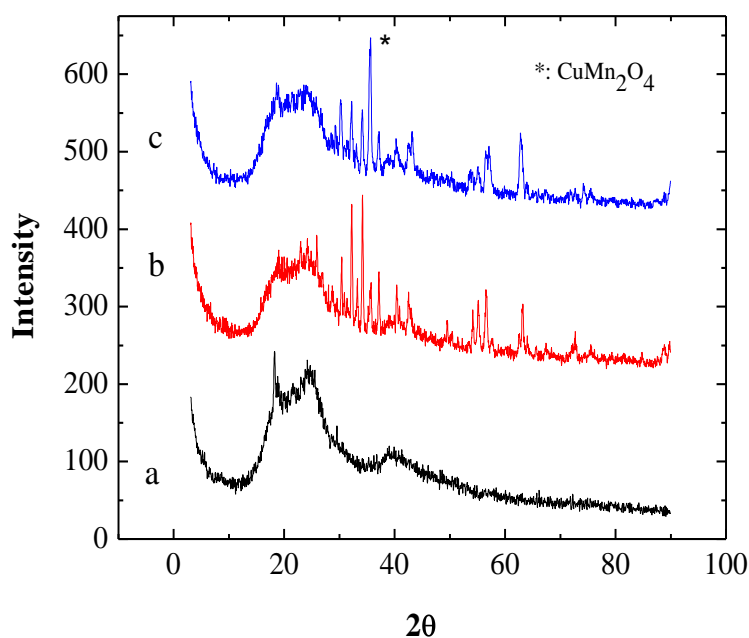

Figure 5.3 XRD patterns of PVC S-39, polymeric composite
materials Reinforced (a) with undoped barium hexaferrite and
(c) with Mn-Cu-Ni barium hexaferrite powders

In other study, it was reported that the peaks for the doped barium ferrite appear approximately at the same position as for the undoped ferrite, but with different intensities. The dopants of Sr, Ni and Mn seem to dissolve in the hexagonal structure. Hexagonal ferrites produced have different types such as M-, W-, Z- and Y-types which has complex crystal and magnetic structure. It was also reported that magnetic ions can be removed by replacing with divalent ions in the literatures (Meshrama, Agrawala, Sinhaa & Misrab, 2004).

5.3 Grain Size Determination

Grain sizes of commercial powder purchased from Aldrich and Mn-Cu-Ni doped barium hexaferrite barium hexaferrite powder were determined. The crystalline size was computed with full width half maximum (FWHM) for these powders. Generally speaking the crystalline sizes of powders werein the range of 33.9 nm and 45 nm.

Table 5.1 Crystalline Size of barium hexaferrite powders

Materials	Grain Size Calculated by X-Pert (nm)
Mn-Cu-Sr doped barium hexaferrite	45.2
Mn-Co Sr doped barium hexaferrite	36.6
Mn-Cu-Ni doped barium hexaferrite	33.9
Mn-Co-Ni doped barium hexaferrite	37.4

5.4 Microstructure

5.4.1 Surface Morphology of Barium Hexaferrite Powders

The average grain size and the shape of Mn-Co-Ni, Mn-Cu-Sr, Mn-Cu-Ni, Mn-Co-Sr doped barium hexaferrite particles were in Figures 5.4, 5.5, 5.6, 5.7 and 5.8. It indicates that M-type ferrite grains are hexagonal-shaped crystals. The critical diameter of the spherical barium ferrite with single magnetic domain is reported to be 460 nm. Since the produced powders were sintered at 1000 ^{o}C, single barium hexaferrite particles were observed in this study. Similar behavior can be seen from elsewhere (Ghasemi, Hossienpour, Morisako, Saatchi & Salehi, 2006). This is why grain growth forms during sintering process as well as agglomeration during preparation of powders.

The microstructure of undoped nano powder that purchased from Aldrich is seen in Figure 5.4. As seen from Figure 5.4, nanoparticle tends to agglomerate either they are sintered or not. Figure 55 shows typical morphology of Mn-Co-Ni doped barium hexaferrite powders. The major microstructure of Mn-Co-Ni doped barium

hexaferrite powders resembles sponge. The microstructure of Mn-Cu-Sr doped barium hexaferrite powders were commonly hexagonal shaped (Figure 5.6). The microstructure of Mn-Cu-Ni doped barium hexaferrite powders seem to mostly agglomerate, but also likely to have a hexagonal structure as seen in Figure 5.7. In the microstructure of Mn-Co-Sr doped barium hexaferrite powder, the hexagonal shape is the major structure (see Figure 5.8).
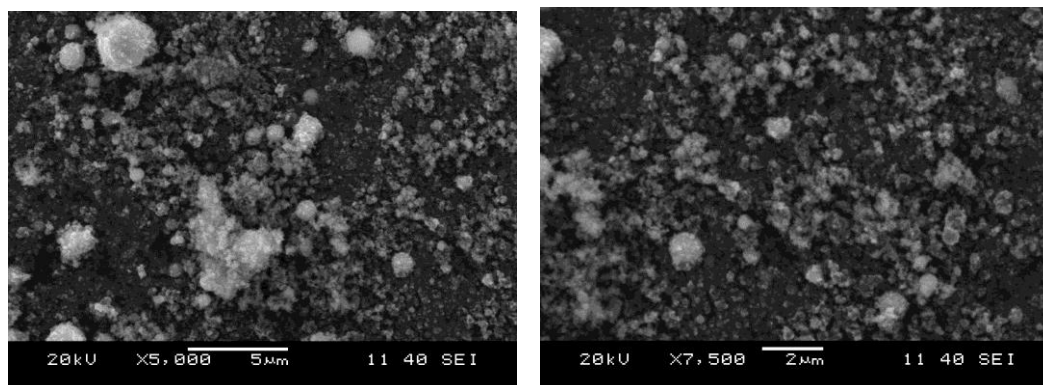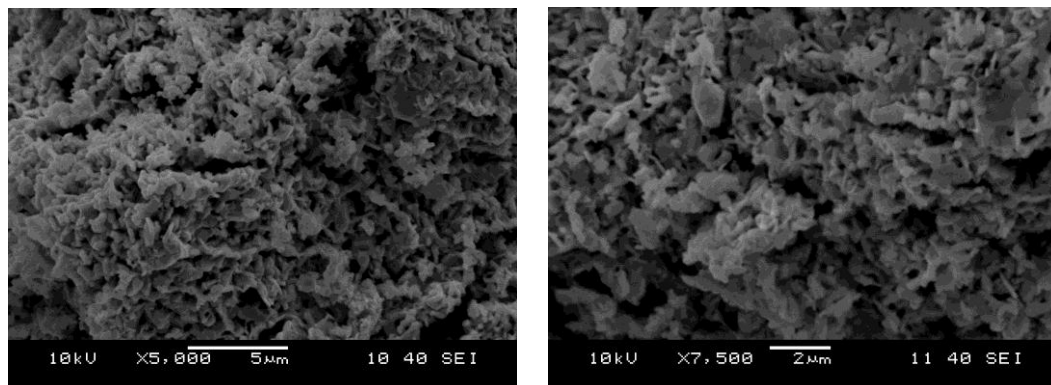

Figure 5.4 Typical morphology of barium hexaferrite nanopowder

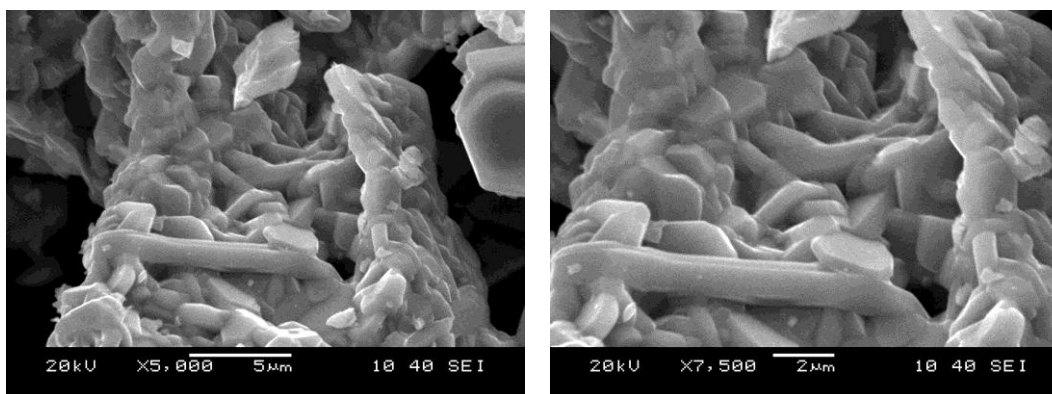Figure 5.5Typical morphology of Mn-Co-Ni doped barium hexaferrite powders

Figure 5.6 Typical morphology of Mn-Cu-Sr doped barium hexaferrite powders
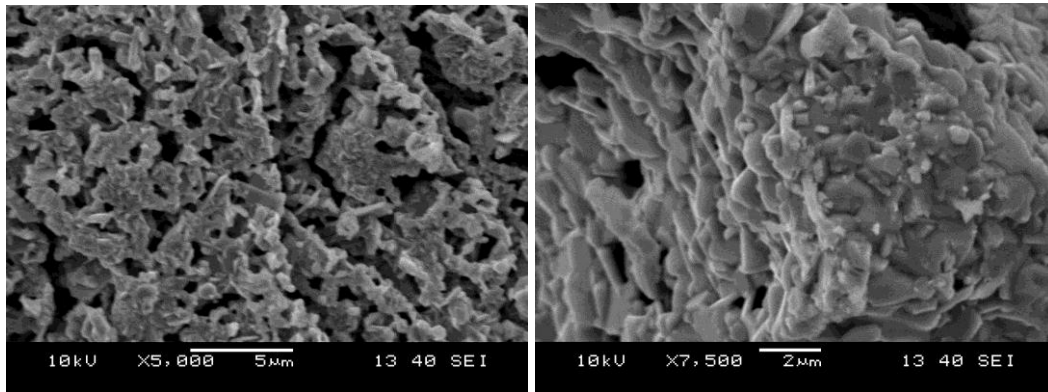
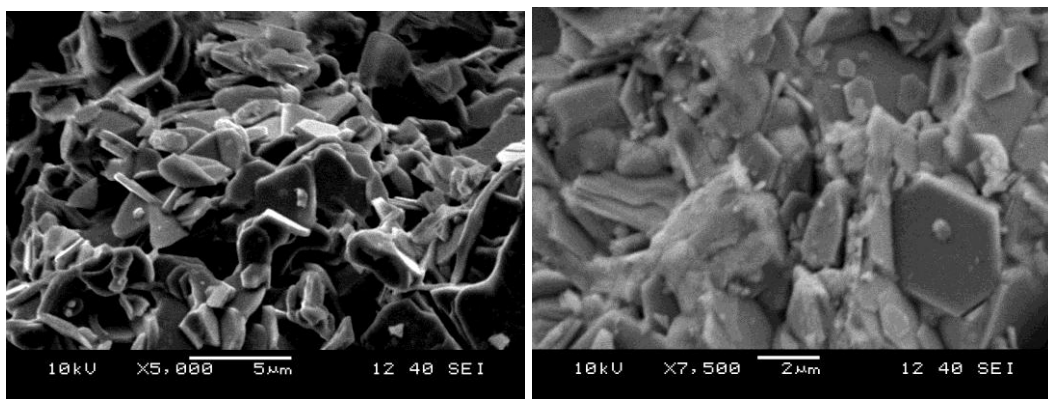Figure 5.7 Typical morphology of Mn-Cu-Ni doped barium hexaferrite powders

Figure 5.8 Typical morphology of Mn-Co-Sr doped barium hexaferrite powders

5.4.2. Surface Morphology of Polymer Nanocomposites

To view the material, electron beam in scanning electron microscope scan on the material. Due to the low glass transition temperature of PVC, electron beam effect the polymer, in some areas when the voltage is 10 kV electron beam melt the polymer. For this reasons EDS or mapping could not be applied on the polymer nanocomposites. Nonetheless as seen in the magnification of 7500x and 10 000x, the homogeneity of the the particles in the nanocomposites was provided with the mixing in the brabender. The particles were dispersed in all the polymer.

Microstructure of sintered barium hexaferrite was studied in many researches. In our study as seen in Figures 5.9 and 5.10. The avarage grain size is 2-4 μm. Gashemi et al. (2006) reported that the average grain size was approximately 7 μm. In addition, Tabatabaie et al. (2008) reported that the average particle size was

approximately 2 μm. Topal (2008) has also indicated that barium hexaferrite that calcined at 1300 ^{o}C possess grains with dimensions up to 7-8 μm. Rezlescu et al. (1999) reported that the critical diameter of the spherical barium ferrite with single magnetic domain is 460 nm. It can be expressed that the barium ferrite particles are not single.
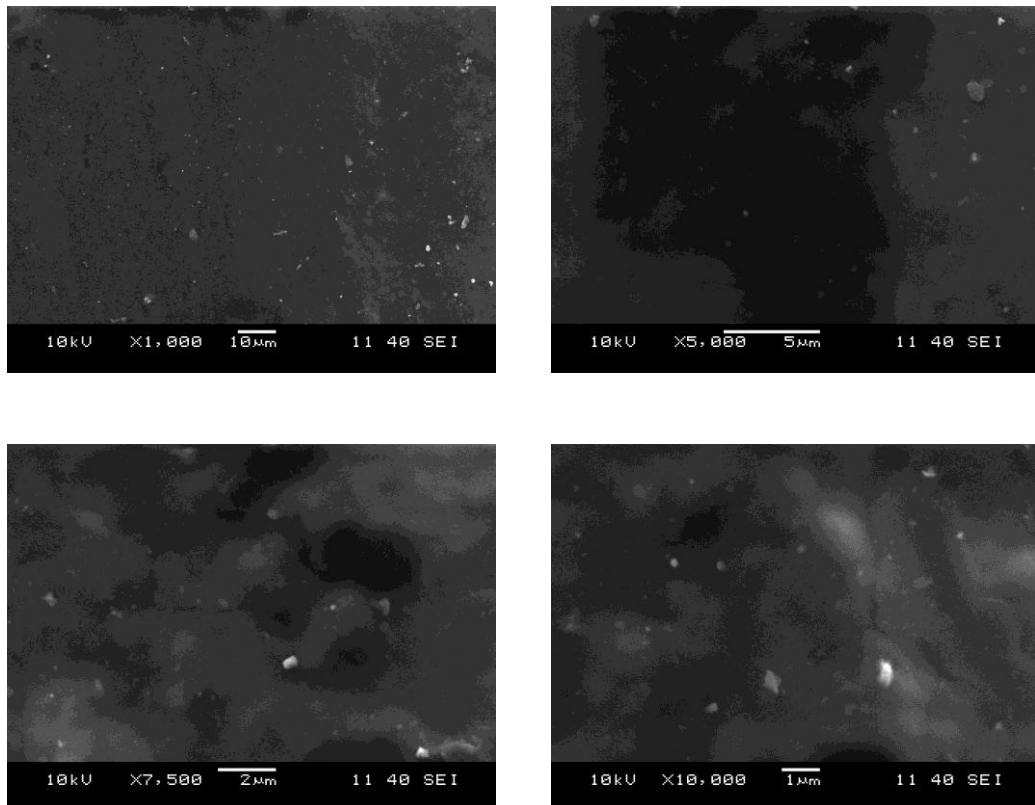

Figure 5.9 Polymer nanocomposites reinforced undoped barium hexaferrite powder

In SEM photographs, Sr enhanced the hexagonal shape of the barium hexaferrite powders. The particle size was measured at the X-Pert using the XRD patterns of undoped barium hexa ferrite and Mn-Cu-Ni doped barium hexa ferrite's FWHM (full width half maximum) of the major peak of the powder. As seen from the results in Figure 5.1 and 4.10 b, X-Pert calculation using the Scherer equation, the calculated particle size is appromately 32 nm for barium hexa ferrite. G.B. Teh. et al. (2007) has calculated the particle size and found that it was nearly 36 nm, and it was also stated that sol-gel method had a smaller range for powder particle size distribution range between 40 and 150 nm. As mentioned in previous studies before, sol-gel method is used to produce smaller particles with a narrower particle size distribution.
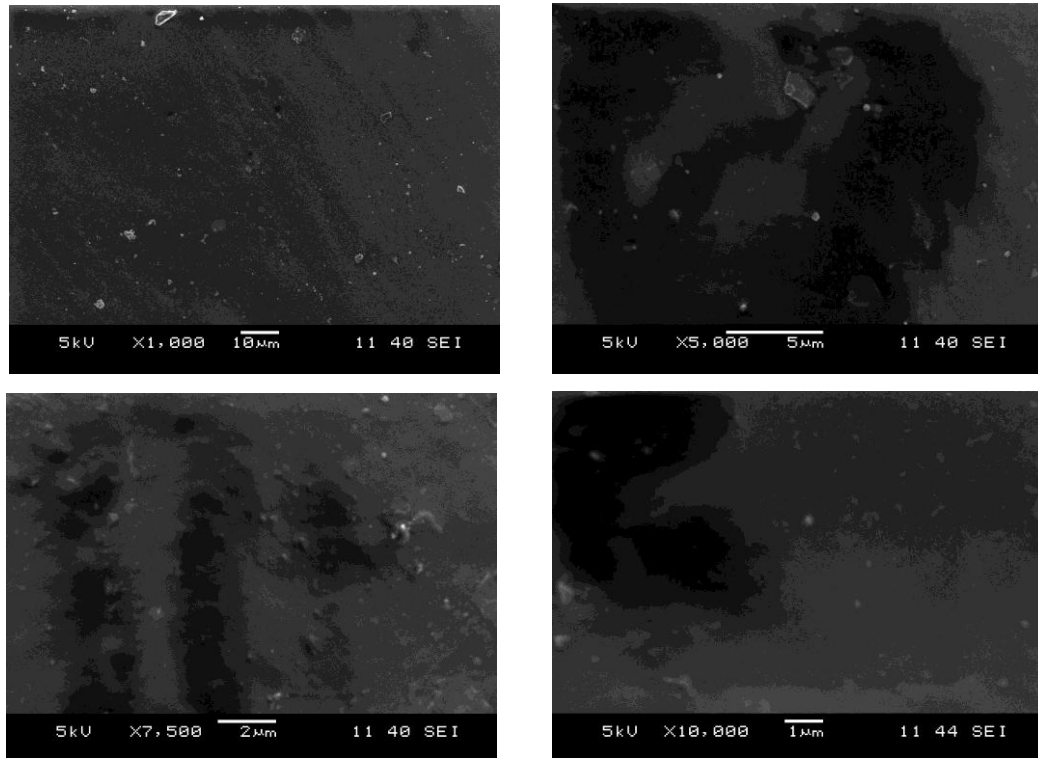
Figure 5.10 Polymer nanocomposites reinforced with Mn-Cu-Ni barium hexaferrite powder

5.5 Mechanical Properties of Polymer Nanocomposites

The DUH results were obtained for PVC, undoped barium ferrite powder reinforced PVC nanocomposite and Mn-Cu-Ni doped barium ferrite powder reinforced PVC. The load was applied three times for both samples. The elasticity modules and the Vickers hardness which are mostly related to each other was measured. As seen from Table 5.2, the results that obtained from raw PVC hardness and elasticity module values are low.

The values that taken from the undoped barium hexaferrite powder reinforced PVC especially from the barium hexaferrite particle were extremely high. The data which was taken from the polymer was lower than the barium hexaferrite particle, but larger than the raw PVC. The load-displacement curve of the undoped barium hexaferrite powder reinforced PVC both taken from the particle and polymer is in Figure 5.12 and 5.13.

Table 5.2 The hardness and elasticity modules of polymer nanocomposites

| Materials	Average Hardness (Vickers)	Average Elasticity Modulus (MPa)
PVC S-39	0.059	8.72
Undoped barium hexaferrite powder reinforced PVC (data was taken from the barium hexaferrite particle)	4.431	713
Undoped barium hexaferrite powder reinforced PVC (data was taken from the polymer)	0.483	77.1
Doped barium hexaferrite powder reinforced PVC (data was taken from the barium hexaferrite particle)	2.542	464
Doped barium hexaferrite powder reinforced PVC (data was taken from the barium hexaferrite polymer)	0.145	35.03
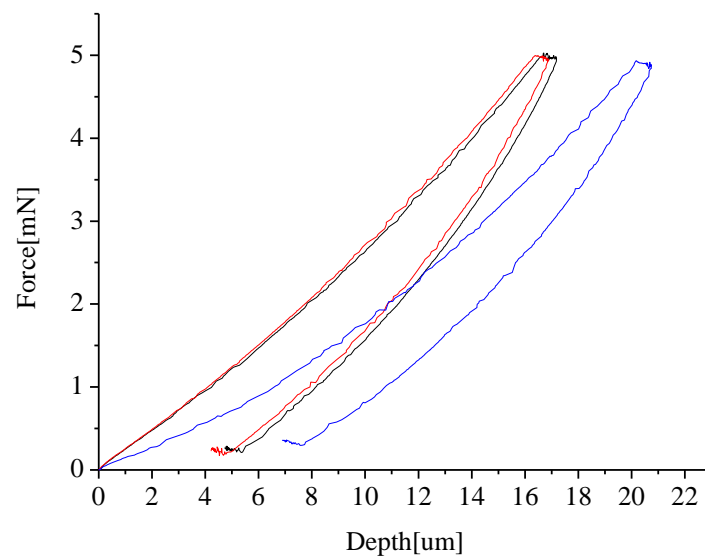
Figure 5.11 The load-displacement curve of the raw PVC

The data that obtained from doped barium hexaferrite powder reinforced PVC, taken either on the barium hexaferrite particle or polymer gave approximately results like the undoped barium hexaferrite powder reinforced PVC. The load-displacement curve of the undoped barium hexaferrite powder reinforced PVC both taken from the particle and polymer is in Figures 5.12 and 5.13.
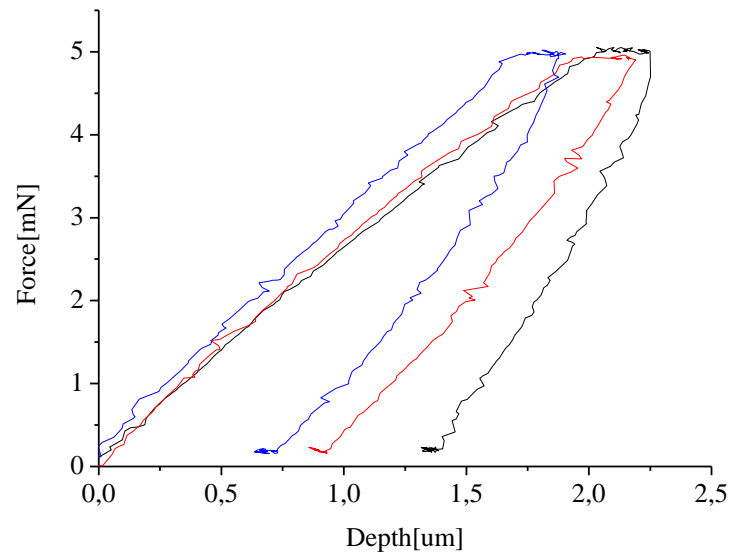
Figure 5.12 The load-displacement curve of barium hexaferrite

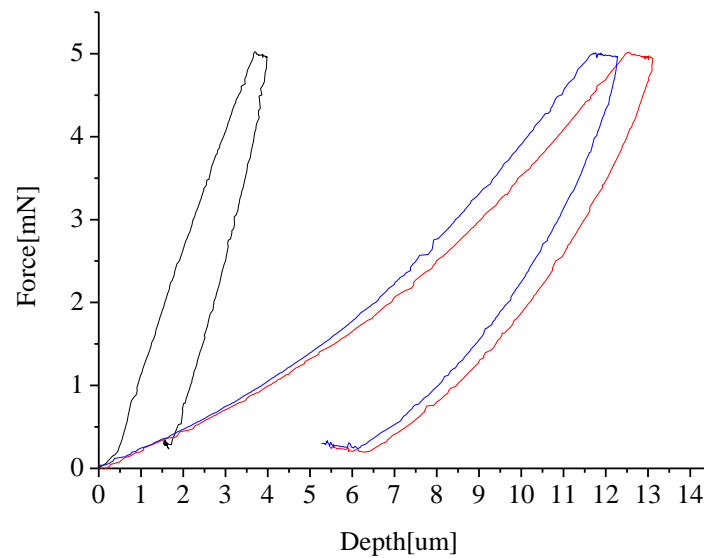particle in polymer nanocomposites (undoped barium hexaferrite)

Figure 5.13 The load-displacement curve of the polymer

in polymer nanocomposites (undoped barium hexaferrite)

As indicated in the table about the hardness and the elasticity modules values raw PVC has the lowest of all as quested. When the magnetic ceramic particles reinforced the PVC, the hardness and elasticity increased at least ten times higher cooperated with the raw PVC. The values that taken from the undoped barium hexaferrite powder's barium hexaferrite particle was extremely high. The data which

was taken from the polymer was lower than the barium hexaferrite particle, but larger than the raw PVC. This situation is also true for the Mn-Cu-Ni doped barium hexaferrite particles that are shown in Figure 5.14 and 5.15 reinforced PVC nanocomposite.
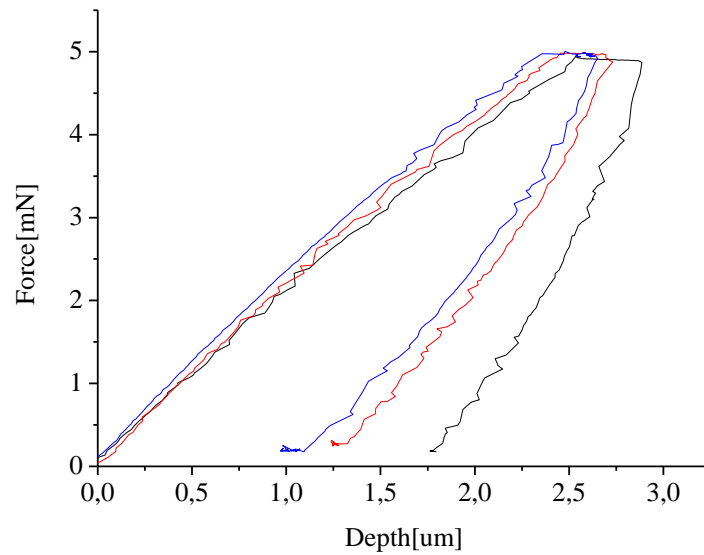

Figure 5.14 The load-displacement curve of the polymer in polymer nanocomposites (doped barium hexaferrite)
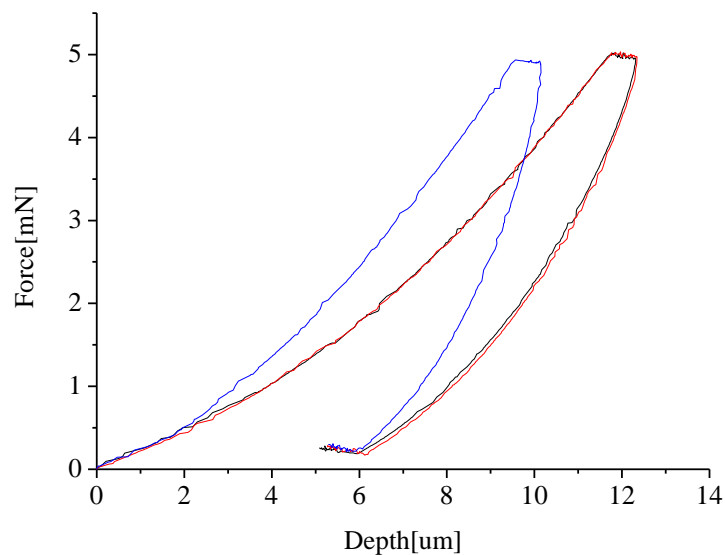

Figure 5.15 The load-displacement curve of the polymer in polymernanocomposites   (doped barium hexaferrite)

With regarding to the results in Table 5.2, particles dispersion in PVC matrix is homogenously as the hardness of the polymer matrix at least 10 times higher than the raw PVC. Therefore, it can be expressed that particles dispersed mostly in whole PVC matrix. It can be strengthen with SEM photographs. The immersed barium hexaferrite particles can be seen from SEM photographs.

5.6 Magnetic Properties

The hysteresis loops of the powders were measured in vibrating sample magnetometer (VSM). The values were obtained both the nanoparticles purchased from Aldrich and the synthesized powders.

The magnetic properties including hysteresis loop, saturation magnetization and coercivity of doped barium hexaferrite was measured in this research with VSM. The hysteresis loop of the samples are presented in Figures 5.16 and 5.17 In addition, Table 5.3 presents the data (H_c, M_s) for the hysteresis loops. It is reported that undoped hexaferrite possesses very high coercive force, which is due to the its uniaxial anisotropy along the c-axis of the M type hexaferrite. In our samples after Mn-Cu-Co-Ni-Sr substituting led to a rapid decrease of H_c according to the reported Hc value for the undoped hexa ferrite, owing to the reduction of magneto crystalline anisotropy. Similar results have also been reported for Mn-Co-Ti substituted barium ferrites by A. Ghasemi et al. (2006), and also reported for Mg-Ti substituted barium ferrite by M. H. Shams et al. (2008) it is expressed that its sharply reduced with change of the easy axis of magnetization from the c-axis to the basal plane.

The magnetic characterization, of both as prepared $BaFe_{12}O_{19}$ and $BaFe_{12-x}(Mn_{0.5}Cu_{0.5}Ni)_{x/2}O_{19})$ reinforced PVC nanocomposites were performed with VSM. The hysteresis loops for $BaFe_{12}O_{19}$ and $BaFe_{12-x}(Mn_{0.5}Cu_{0.5}Ni)_{x/2}O_{19})$ reinforced PVC nanocomposites are shown in the Figure 5.18. Comparing the results of polymer nanocomposites with the hysteresis loops of undoped barium hexaferrite powder and Mn-Cu-Ni doped barium hexaferrite powder, they fortify each other with the value of H_c.
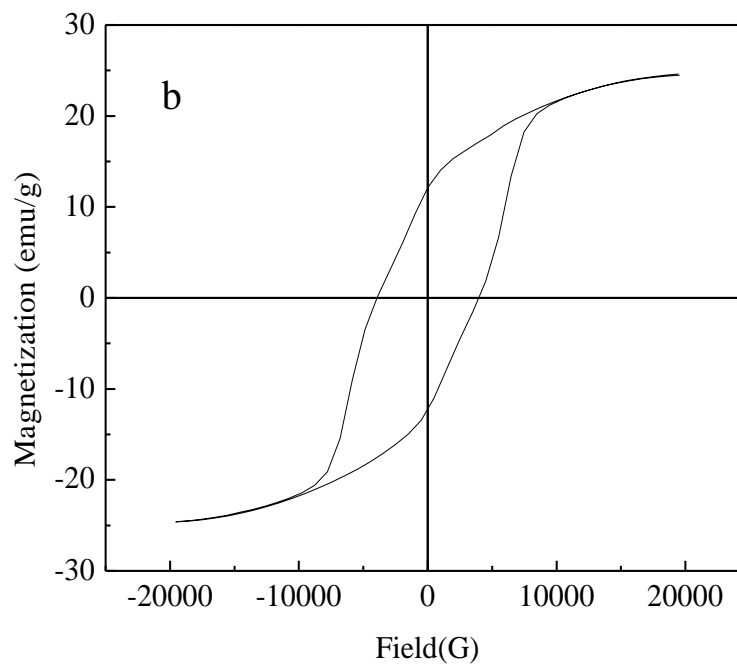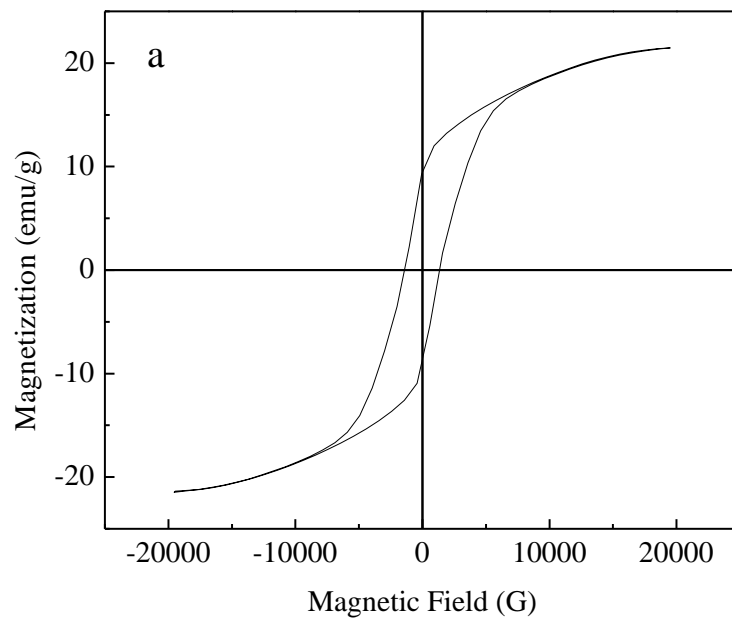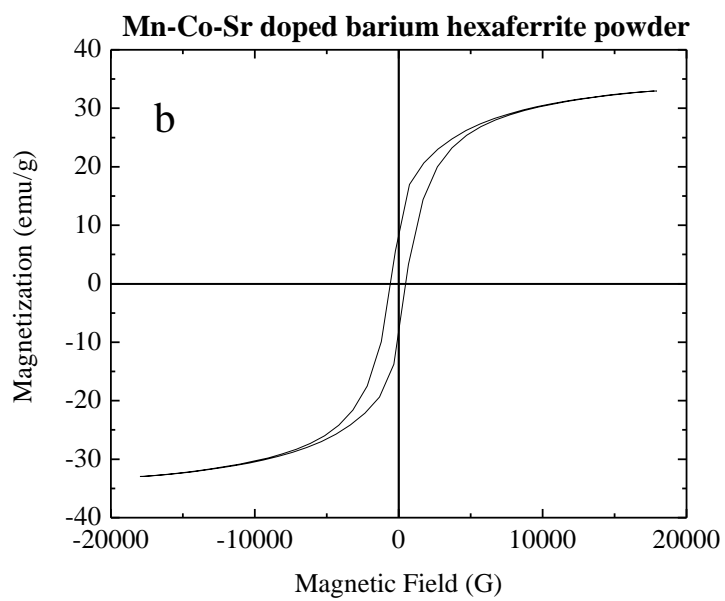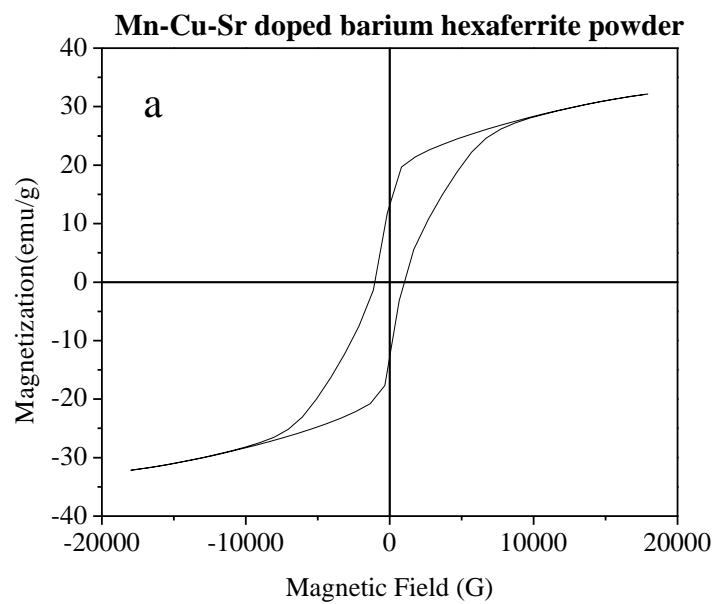
Figure 5.16 The hysteresis loops of (a) undopped barium hexaferrite

(b) Purchased barium hexaferrite

Mn-Cu-Sr doped barium hexaferrite powder

a

Mn-Co-Sr doped barium hexaferrite powder

b

Mn-Cu-Ni doped barium hexaferrite powder

Mn-Co-Ni doped barium hexaferrite powder
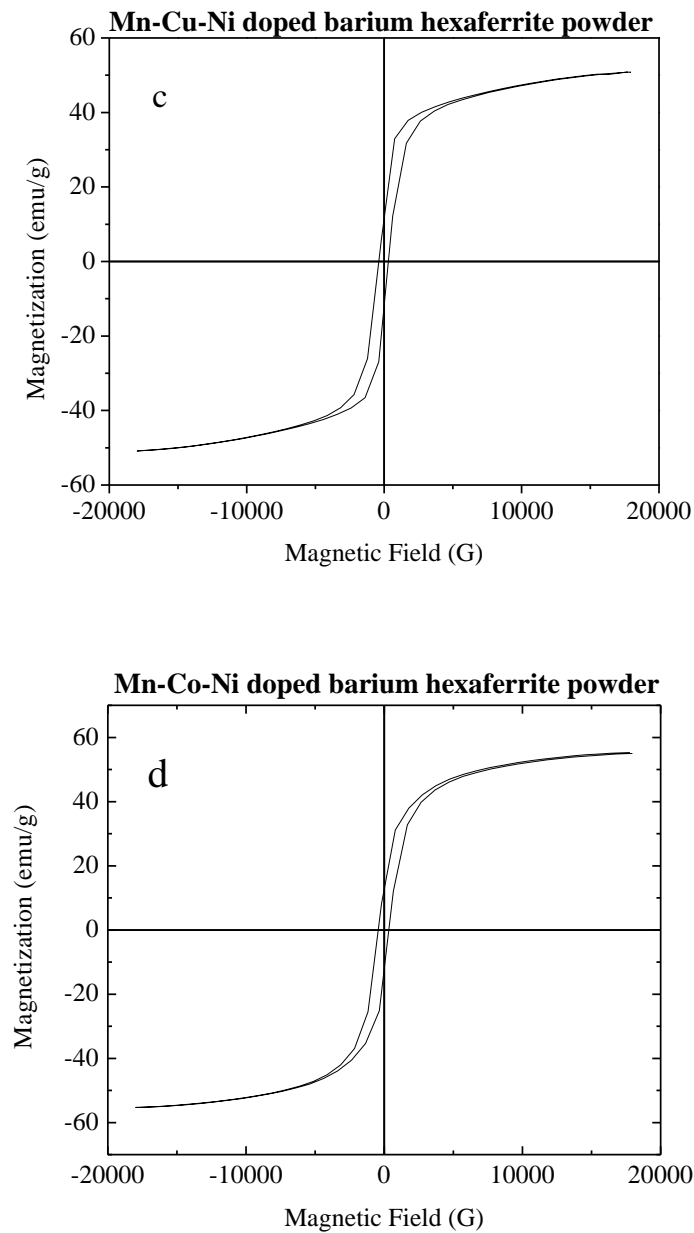
Figure 5.17 The hysteresis loops of a) Mn-Cu-Sr b) Mn-Co-Sr

c) Mn-Cu-Ni   d) Mn-Co-Ni

The magnetic characterization for both as synthesized $BaFe_{12}O_{19}$, $BaFe_{12-x}(Mn_{0.5}Co_{0.5}Sr)_{x/2}O_{19}$, $BaFe_{12-x}(Mn_{0.5}Co_{0.5}Ni)_{x/2}O_{19}$, $BaFe_{12-x}(Mn_{0.5}Cu_{0.5}Ni)_{x/2}O_{19}$ and $BaFe_{12-x}(Mn_{0.5}Cu_{0.5}Sr)_{x/2}O_{19}$ was carried out through VSM. The hysteresis loop of the samples are presented in Figure 5.16 a and Figure 5.17 (a-d). In addition Table 5.3 presents the data (H_c and M_s) for the

hysteresis loops. It is reported that undoped hexa ferrite possesses very high coercive force which is due to the its unaxial anisotropy along the c-axis of the m type hexaferrite. In our samples after Mn-Cu-Co-Ni-Sr substituting led to a rapid decrease of H_c according to the reported H_c value for the undoped hexaferrite, owing to the reduction of magnetocrystalline anisotropy. Similar results have also been reported for Mn-Cu-Ti substituted barium ferrites by (Ghasemi, Saatchi, 2006).

Tablo 5.3 M_s and H_c values of barium hexaferrite powders.

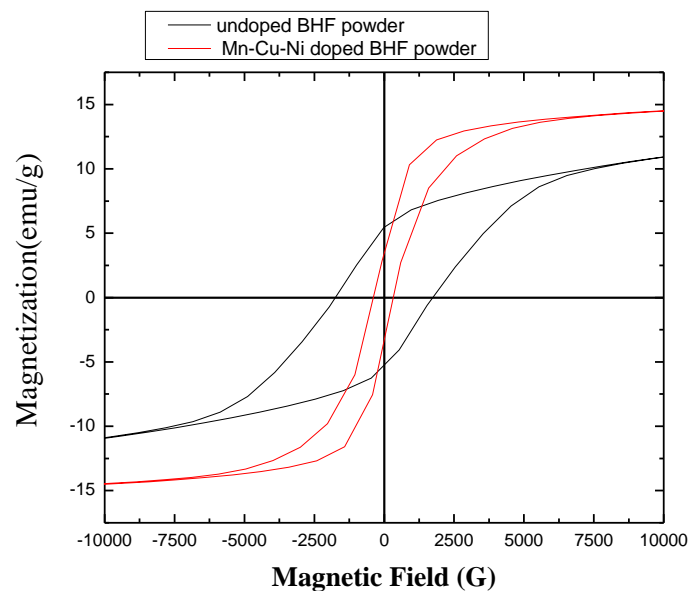| Materials	Magnetic Saturation(emu/g)	Coersivity (Oersted)
Purhased nanopowder (Aldrich)	34,38	3939.8
Undoped barium hexaferrite powder	25.03	1381.8
Mn-Cu-Sr doped barium hexaferrite powder	32,07	1036,3
Mn-Co-Sr doped barium hexaferrite powder	32,66	533,72
Mn-Cu-Ni doped barium hexaferrite powder	50,68	349,80
Mn-Co-Ni doped barium hexaferrite powder	55,16	380,82

Figure 5.18 The hysteresis loop of undoped and doped barium hexaferrite powder reinforced polymer nano composite

Table 5.4 M_s and H_c values of polymer nanocomposites

Materials	H_c (coercivity) gauss	M_s (magnetic saturation) emu/g
Undoped barium hexaferrite polymer nanocomposites	1832,34	13.97
Barium hexaferrite from Aldrich polymer nanocomposites	302.36	10.66

M. H. Shams et al. (2008) also reported that for Mg-Ti substituted barium ferrite the high value of H_c with about 258.7 kA/m for the undoped barium hexaferrite powders is due to the change of the easy axis of M-type hexaferrite. The reduction of the H_c for dopped hexaferrite about 6.1 kA/m is due to the change of the easy axis of magnetization from the c-axis to the basal plane. A. Ghasemi et al. (2006) advocated the results that indicated in M.H. Shams et al. (2008). In addition that substitution elements cause the incensement of H_c. G. B. Tech et al. (2007) pointed out that Co(II) substitution in $BaFe_{12}O_{19}$ reduced the coercivity from 1082 G mg^{-1} to 275,8 G mg^{-1}. The hysteresis loss area in the cobalt (II) - subsituted barium hexaferrite is smaller than the undoped one.

CHAPTER SIX
CONCLUSION AND FUTURE PLAN

6.1 General Results

In this study, production and characterization of barium hexaferrite powders and polymer nanocomposites reinforced with barium hexaferrite powders were investigated. Important results obtained from this study are as follows;

The heat treatment regime was determined with the DTA-TGA results. As the phase formation temperature was found to be 1000 ^{o}C, concerning with the weight loss of the powders did not continue above this temperature.

It can be clearly seen from XRD results that the required phases mostly obtained which directly affects the magnetic properties. Due to the different phases obtained such as $NiFe_2O_4$, $Ba_{0.5}Sr_{0.5}Fe_{12}O_{19}$, $CuMn_2O_4$ and Fe_2O_3, they do not affect the magnetic properties as understood from the literature results.

From SEM analysis, barium hexaferrite powders mostly resemble to have hexagonal structure or tend to have hexagonal structure. Sr enhanced the hexagonal structure of barium hexaferrite powders. Also from the SEM examinations of polymer nanocomposites, it can be expressed that particles homogenously dispersed in polymer.

The DUH results explains as the SEM photographs that from the elasticity modulus and hardnesses of polymer nanocomposites, barium hexaferrite particles were dispersed homogenously. The value of hardness and elasticity modules of polymer nanocomposites at least ten times larger than the raw polymer. Thus the results indicate that barium hexaferrite powders are homogenously in the nanocomposites distributed.

The VSM results have good agreement with literature. The doping elements decreased the coercivity. As the coersivity values of undoped barium hexaferrite powders are larger than the doped powders. The coersivity value was found about 1381 oersted for the undoped barium hexaferrite powders and about 400 oersted for the doped barium hexaferrite powders.

6.2. Future Plan

It is recommended that heat treatment conditions for barium hexaferrite powder should be carried out in order to obtain more homogenous phases for good magnetic properties. With this aim new heat treatment conditions occurs hexagonal micro structure as seen in the literature. Different polymer nanocomposites can be produced in different barium hexaferrite: Polymer ratios concerning with the literature.

REFERENCES

Carp, O., Barjega, R.,Segal, E., & Brezeanu, M. (1998). Nonconventional method for obtaining hexaferrites II. Barium hexaferrite, *Thermochimica Acta*, 318, 57- 62.

Dokumacı, E., *Investigation of high and low tempertaure corrosion behavior of nickel – base alloys*. The Graduate School of Natural and Applied Sciences of Dokuz Eylül University Master Thesis, 2006

Dong, L., Han, Z., Zhang, Y., Wu, Z., & Zhang, Z., (2006). Synthesis of hexagonal barium ferrite nano particle by sol-gel method. *Rare Metals Spec. Issue*, 25, 605-608.

Fischer, H., (2003). Polymer nano-composites: from Fundamentals research to specific applications. *Materials Science and Engineering C*, 23, 763-772.

Gacitua, E., Ballerini, A. A. & Zhang, J. (2005). Polymer Nanocomposites: Synthetic and Natural Fillers A Review. *Clencia Y Technologia*, 7(3), 159-178.

Gao, F. (2004). Clay/polymer composites: the story. *Materials Today*, 50-55.

Ghasemi, A., Liu, X., & Morisako, A., (2007). Magnetic and microwave absorption properties of $BaFe_{12-x}$, $(Mn_{0.5}Cu_{0.5}Zr)_{x/2}O_{19}$ synthesized by sol–gel processing. *Journal of Magnetism and Magnetic Materials*, 316, e105–e108.

Ghasemi, A., Hossienpour, A., Morisako, A., Saatchi, A., & Salehi, M. (2006). Electromagnetic properties and microwave absorbing characteristics of doped barium hexa ferrite. *Journal of Magnetism and Magnetic Materials*, 302, 429-435.

Ghasemi, A., Saatchi, A., Salehi, M., Hossienpour, A., Morisako, A., & Liu, X., (2006). Magnetic characteristics of Mn–Co–Ti substituted barium ferrite synthesized by sol–gel processing. *Phys. Stat. Sol.,* (a) 203-10, 2513–2521.

Gitam University (2009) Retrieved May 2009 From http://www.gitam.edu/eresource/nano/NANOTECHNOLOGY/bottamup%20app.htm

Gupta, S., Sajdha, Sheikh, H.N., Kalsotra, Kumar, N., & Kumar, S. (2008). Magnetic Nanocomposites of Mixed Oxides of Iron and Barium Synthesized under Different Oxidative Environments. *Inorganic Materials*, 44, 990-1008.

Holister, P., Weener, J.W., Roman, C., & Harper, T., (2003). Nanoparticles. *Technology White Papers*, 3, 3-11.

Japan Petroleum Energy Center, 2006, Retrieved May 2009 from http://www.pecj.or.jp/english/jcap/jcap2/jcap2_05.html

Jordan, J., Jacob, K. I., Tannenbaum, R., Sharaf, M. A., & Jasiyk, I. (2005). Experimental Trends in Polymer Nanocomposites. *Materials Science and Engineering*, A 393, 1-11.

Koutzarova, T., Kolev, S., Ghelev, C., Grigorov, K., & Nedkov, I., (2008). Structural and magnetic properties and preparation techniques of nanosized M-type hexaferrite powders. *Advances in Nanoscale Magnetism, Springer Proceedings in Physics*,122, 183

Mai, Y. W., & Yu Z. Z., (Eds.). (2006). Polymer Nanocomposites. Cambridge: Woodhead Publishing Limited.

Meshrama, Agrawala, Sinhaa & Misrab, 2004, Retrieved May 2009 from https://soar-ir.shinshu-u.ac.jp/dspace/bitstream.

Meshrama, M.R., Agrawala, N.K., Sinhaa, B., & Misrab, P.S. (2004). of M-type barium hexagonal ferrite-based wide band microwave absorber. *Journal of Magnetism and Magnetic Materials*, 271, 207–214.

Moulson, A.J., & Herbert, J.M., (2003). *Electroceramics materials, properties, applications (2)*. (469-544) England: John Wiley.

Okamoto, M. (2005). Biodegradable polymer/layered silicate nanocomposites: *Handbook of Biodegradable Polymeric Materials and Their Applications* (1-45). USA: American Scientific Publishers.

Pinho, M. S., Caffarena, V. R., Lima, R. C., Capitaneo, J. L. & Ogasawara T. (2005). Microwave absorption of substituted m-type barium hexa ferrite nano powders in polychloroprene matrices. *2nd Mercosur Congress on Chemical Engineering*

Pramanik, N.C., Fujii, T., Nakanishi, M., Takada, J., & Seok, S.I. (2006). The effect of heat treatment temperature on the microstructure and magnetic properties of $Ba_2Co_2Fe_{12}O_{22}$ (Co_2Y) prepared by sol–gel method. *Materials Letters*, 60, 2718–2722.

Rezlescu, L., Rezlescu, E., Popa, P.D., & Rezlescu, N. (1999). Fine barium hexaferrite powder prepared by the crystallization of glass. Journal of Magnetism and Magnetic Materials, 193, 288-290.

Sahin, O., Uzun, O., Kölemen, U., & Ucar, N. (2008). Mechanical characterization for β-Sn single crystals using nanoindentation tests. *Materials Characterization,* 59, 427-434.

Shams, M. H., Salehi, S. M. A., & Ghasemi, A. (2008). Electromagnetic wave absorption characteristic of Mg-Ti substituted Ba- hexaferrite, *Materials Letter,* 62, 1731-1733.

Somiya, S., & Roy, R., (2000). Hydrothermal synthesis of fine oxide powders. *Bull. Mater. Sci.*, 23-6, 453-460.

Tabatabaie, F., Fathi, M. H., Saatchi, A., & Ghasemi, A. (2009). Microwave absorption properties of Mn- and Ti- doped strontium hexa ferrite. *Journal of Alloys and Compounds*, 470, 332-335.

Teh, G. B., Nagalingam, S., & Jefferson, D. A. (2007). Preparation of Co(II) and Co(III)- substituted barium ferrite prepared by sol-gel method. *Material Chemistry and Physics*, 101, 158-162.

Teh, G. B., Nagalingam, S., & Jefferson, D. A. (2007). A study of magnetoplumbite-type (M-type) cobalt-titanium-substituted barium ferrite, $BaCo_xTi_xFe_{12-2x}O_{19}$ (x=1-6). *Material Chemistry and Physics*, 105, 253-259.

Topal, U., (2008). Factors influencing the remanent properties of hard magnetic barium ferrites: Impurity phases and grain sizes. *Journal of Magnetism and Magnetic Materials*, 320, 331-335.

Vahaplar, K., *Structural and magnetic properties of Si (100)/Ta/Co multilayers for spintronics applications*. The Graduate School of Engineering and Sciences of İzmir Institute of Technology Master Thesis, 2007

Vaia, R. A. (2002). Polymer nanocomposites open a new dimension for plastics and composites. *The AMPTIAC Newsletter*, 6-1, 17-24.

Winey, K. I., & Vaia, R. A. (2007). *Polymer Nanocomposites. Mrs Bulletin*, 32, 314-322.

Winterer, M. (2007) Chemical Vapour Synthesis Of Nanocrystalline Powders, Retrieved May 2009 from http://www.uni-due.de/ivg/nano/synthesis_nppt.shtml.

Zhang, H., Liu, Z., Ma, C., Yao, X., Zhang, L., & Wu, M., (2002). Complex permittivity, permeability, and microwave absorption of Zn- and Ti-substituted barium ferrite by citrate sol/gel process. *Materials Science and Engineering B96*, 289-295

Zhong, W., Ding, W., Zhang, N., Hong, J., Yan, & Q., Du, (1997). Step in synthesis of ultrafine $BaFe_{12}0_{19}$ by sol-gel technique. *Journal of Magnetism and Magnetic Materials*, 168, 196-202.